Low-loss Metasurface Optics down to the Deep Ultraviolet Region

Cheng Zhang[1,2,3†,*], Shawn Divitt[2,3†], Qingbin Fan[4†], Wenqi Zhu[2,3], Amit Agrawal[2,3], Yanqing Lu[4], Ting Xu[4*] and Henri J. Lezec[2,*]

[1.] School of Optical and Electronic Information & Wuhan National Laboratory for Optoelectronics, Huazhong University of Science and Technology, Wuhan, 430074, China.

[2.] Physical Measurement Laboratory, National Institute of Standards and Technology, Gaithersburg, MD, 20899, USA.

[3.] Maryland Nanocenter, University of Maryland, College Park, MD, 20742, USA.

[4.] National Laboratory of Solid State Microstructures, College of Engineering and Applied Sciences and Collaborative Innovation Center of Advanced Microstructures, Nanjing University, Nanjing, 210093, China.

[†] Equal contributors

[*] Corresponding authors. Cheng Zhang, Email: cheng.zhang@hust.edu.cn; Ting Xu, Email: xuting@nju.edu.cn; Henri J. Lezec, Email: henri.lezec@nist.gov

Abstract

Shrinking conventional optical systems to chip-scale dimensions will benefit custom applications in imaging, displaying, sensing, spectroscopy, and metrology. Towards this goal, metasurfaces — planar arrays of subwavelength electromagnetic structures that collectively mimic the functionality of thicker conventional optical elements — have been exploited at frequencies ranging from the microwave up to the visible. Here, we demonstrate high-performance metasurface optical components operating at ultraviolet frequencies, including down to the record-short deep ultraviolet range, and performing representative wavefront shaping functions, namely high-numerical-aperture lensing, accelerating beam generation, and hologram projection. The constituent nanostructured elements of the metasurfaces are formed of hafnium oxide — a loss-less, high-refractive-index dielectric material deposited using low-temperature atomic layer deposition and patterned using high-aspect-ratio Damascene lithography. This study opens the way towards low-form-factor, multifunctional ultraviolet nanophotonic platforms based on flat optical components, enabling diverse applications including lithography, imaging, spectroscopy, and quantum information processing.

Introduction

An optical metasurface is a planar array of subwavelength electromagnetic structures that emulate the operation of a conventional refractive, birefringent, or diffractive optical component such as a lens, waveplate, or hologram, through individually tailored amplitude, phase, or polarization transformations of incident light[1-9]. Dielectric materials such as amorphous Si[10, 11], polycrystalline Si[12], titanium dioxide (TiO_2)[13, 14], and gallium nitride (GaN)[15, 16] have been used to realize metasurfaces operating at infrared and visible frequencies. The scarcity of dielectric materials that are characterized by low optical loss at higher frequencies and simultaneously amenable to high-aspect-ratio nanopatterning, has impeded the development of metasurfaces for applications in the ultraviolet (UV) range, a technologically important spectral regime hosting diverse applications in lithography, imaging, spectroscopy, time keeping, and quantum information processing[17-19]. To date, metasurfaces designed for operation in the near-UV (UV-A; free-space wavelength range: 315 nm $\leq \lambda_0 \leq$ 380 nm; energy range: 3.26 eV $\leq E_0 \leq$ 3.94 eV) have recently been implemented using niobium pentoxide (Nb_2O_5), down to an operation free-space wavelength λ_0 = 355 nm[20]. Crystalline Si has been used to realize metasurfaces operating down to λ_0 = 290 nm[21], a wavelength falling within the mid-UV (UV-B; 280 nm $\leq \lambda_0 \leq$ 315 nm; 3.94 eV $\leq E_0 \leq$ 4.43 eV), but the device efficiencies remain limited by the severe absorption loss associated with illumination frequencies above the bandgap of Si ($E_g \approx$ 1.1 eV). In both studies, the demonstrated functionalities are limited to hologram generation and beam deflection, while other important wavefront shaping functionalities that can be empowered by optical metasurfaces, such as high-numerical-aperture focusing and structured beam generation, are not achieved yet. Meanwhile, metasurfaces able to operate at even higher frequencies, such as within the deep-UV range (longer wavelength portion of UV-C; 190 nm $\leq \lambda_0 \leq$ 280 nm; 4.43 eV $\leq E_0 \leq$ 6.53 eV), have not been realized due to the challenge of identifying a dielectric material that both has a suitably low optical absorption coefficient in that range and can be patterned into high-aspect-ratio nanostructures using available nano-fabrication techniques.

Here, we report on high-performance dielectric metasurfaces operating over a broad UV range, including within the record-short, deep-UV regime, and performing representative wavefront shaping functionalities. The constituent nanostructured elements of the metasurfaces are formed of hafnium oxide (HfO_2) — an UV-transparent, high-refractive-index dielectric material. Although HfO_2 has been commonly exploited as a high static dielectric constant (high-κ) material in integrated circuit fabrication[22, 23], its applications in optical devices have largely been limited to optical coatings based on planar thin films. This is due to the difficulty of patterning HfO_2 into high-aspect-ratio nanostructures. In this work, we overcome this limitation and exploit, for the first time, the material's applications in meta-devices operating in the UV and the deep-UV regime. We deposit high-quality, UV-transparent HfO_2 films using low-temperature atomic layer deposition (ALD) and pattern the films using a high-aspect-ratio, resist-based Damascene lithography technique[24-26]. We implement metasurfaces designed for operation at the three representative UV wavelengths of 364 nm, 325 nm, and 266 nm, which perform a variety of optical functions, namely high-numerical-aperture lensing, accelerating beam generation, and hologram projection, including under spin control for the last two applications. This achievement opens the way for low-form-factor and multifunctional photonic systems based on UV flat optics, and suggests promising applications in photolithography, high-resolution imaging, UV spectroscopy and quantum information processing.

Results

Material choice and fabrication approach. The implemented metasurface devices consist of HfO_2 nanopillars of either circular or elliptical in-plane cross-sections (Fig. 1a), densely arrayed on a transparent UV-grade fused silica substrate of low refractive index (Supplementary Information, Fig. S1). The choice of HfO_2 — a material most commonly exploited for its high static dielectric constant as transistor gate insulator in complementary metal oxide semiconductor (CMOS) integrated circuits — is guided by the promise of both a large refractive index (n > 2.1 for λ_0 < 400 nm) and a wide bandgap E_g = 5.7 eV (λ_g = 217 nm) located well within the deep-UV, leading to a negligible extinction coefficient ($k \approx 0$) for $\lambda_0 \geq \lambda_g$. Though the requirement of nanopillar dimensions of wavelength-scale height (several hundred nanometers), subwavelength-scale in-plane circle diameter or ellipse minor axis (few tens of nanometers), and vertical sidewalls suggest that pattern transfer with a directional dry-etching technique such as reactive ion etching would be optimal, we were unable to identify a suitable dry-etch chemistry for HfO_2 (a material commonly patterned by non-directional wet chemical etching[27]). We instead explore the use of Damascene lithography[24-26] for HfO_2 metasurface fabrication, a process that involves first patterning resist using electron beam lithography, conformally filling the open volumes of the resist template with HfO_2 using atomic layer deposition (ALD), back-etching the over-coated HfO_2 layer using argon (Ar) ion milling, and finally removing the remaining resist with solvent to form the required high-aspect-ratio nanopillars (see Materials and methods).

Preservation of the physical integrity of the resist template implies use of a plasma-free thermal ALD process having a process temperature, T_p, lower than the glass transition temperature (reflow temperature) of the utilized resist, T_g, along with a process chemistry having by-products that are not corrosive to the resist. Fulfilling both process tolerance requirements rules out the use of common Hf precursors such as Tetrakis(ethylmethylamino)Hafnium (TEMAH)[28], for which the minimum T_p ($\approx$ 150 °C) is significantly greater than the T_g of common electron beam (e-beam) resists, or Hafnium Chloride ($HfCl_4$)[29], for which the reaction by-product (HCl) attacks the resist. Instead, we investigate Tetrakis(dimethylamino)Hafnium (TDMAH)[30] as an alternative Hf precursor for thermal ALD of high-optical-quality HfO_2, using a T_p below that of the T_g of common e-beam organic resists (such as ZEP, for which $T_g \approx 105$ °C). To avoid the risk of incomplete reaction cycles and physical condensation of precursors associated with low-temperature ALD (yielding films having defects and voids, and hence, degraded sub-bandgap optical properties, such as reduced refractive index n and finite extinction coefficient k), an existing ALD process using TDMAH and H_2O precursors and operating at T_p = 200 °C is modified (Fig. 1b) by (1) decreasing the process temperature to T_p = 95 °C; (2) increasing the TDMAH pulsing time, t_1, from 0.25 s to 1 s, to enable a complete reaction with the OH monolayer resulting from the previous cycle; and (3) increasing N_2 purging times, t_2 and t_4, from 12 s to 75 s, to ensure a full removal of excessive precursors and reaction byproducts (see Materials and methods). As revealed by x-ray diffraction characterization (Supplementary Information, Section II) and spectroscopic ellipsometry measurements (Fig. 1c and Supplementary Information, Section III), hafnium oxide films deposited using the modified low-temperature ALD process are respectively amorphous and characterized by a high refractive index (n > 2.1) and negligible optical loss ($k \approx 0$), over an UV wavelength interval 220 nm $\leq \lambda_0 \leq$ 380 nm spanning the full mid- and near-UV ranges, as well as more than half of the deep-UV range. The measured wavelength dependences of n and k closely match those of a film grown using the 200 °C reference ALD process (Supplementary Information, Fig. S4), demonstrating that the optical quality of the deposited HfO_2

can be maintained at significantly lower ALD process temperatures with choice of a suitable Hf precursor and proper adjustment of pulsing and purging times. Note that the 95°C-ALD-deposited HfO_2 films exhibit a high refractive index (n > 2.0) and zero optical loss ($k = 0$) in the visible range (380 nm $\leq \lambda_0 \leq$ 800 nm), making it suitable for fabricating low-loss metasurface devices in this wavelength range as well (Supplementary Information, Fig. S5).

Using ZEP resist for electron beam lithography and the low-temperature TDMAH-based ALD process for hafnium oxide deposition, the proposed Damascene fabrication process is applied to yield defect-free metasurfaces each consisting of a large array of densely packed HfO_2 nanopillars on a UV-grade fused silica substrate (Fig. 1f). Nanopillars have uniform height, circular (Fig. 1d) or elliptical (Fig. 1e) in-plane cross sections, and are characterized by straight, vertical and smooth sidewall (Figs. 1d and 1e, and Supplementary Information, Figs. S7 to S11). The nanopillar rotation angle and two principle axis lengths in the plane of the metasurfaces (respectively, θ, D_1, and D_2, where θ = 0 and $D_1 = D_2 = D$ in the case of a circular cross-section), vary as a function of nanopillar position (with $0 \leq \theta < \pi$ and 50 nm $\leq (D_1, D_2) \leq$ 160 nm) depending on the optical function implemented by the metasurface. The nanopillar height H varies depending on the operation wavelength of the metasurface (400 nm $\leq H \leq$ 550 nm).

We first demonstrate lenses, self-accelerating beam generators, and holograms based on polarization-independent metasurfaces having nanopillars of in-plane circular cross-sections, that operate at near-UV wavelengths of 364 nm and 325 nm (corresponding to emission lines of an argon-ion and a helium-cadmium laser, respectively) with efficiencies up to 72 %. Further exploiting the high patterning fidelity of the Damascene technique and leveraging the negligible optical loss of the as-deposited HfO_2 dielectric material across most of the ultraviolet regime, we scale down metasurface critical dimensions to realize polarization-independent holograms operating at a deep-UV wavelength of 266 nm (corresponding to the emission line of an optical parametric oscillator pumped by a nanosecond Q-switched Nd:YAG laser), moreover with relatively high efficiencies (> 60 %). Finally, by opening up the design space with the three degrees of freedom provided by elliptically-shaped nanopillars (θ, D_1, and D_2), compared to the single degree of freedom allowed by circularly-shaped nanopillars (D), we realize spin-multiplexed metasurfaces that impart independent phase shift profiles to light emerging from the device, under illumination with left-handed circularly-polarized (LCP) or right-handed circularly-polarized

(RCP) light, respectively. The implemented self-accelerating beam generators and spin-multiplexed metaholograms operate at UV wavelengths of 364 nm and 266 nm, respectively, with efficiencies up to 61 %.

Polarization-independent ultraviolet metasurfaces. Each polarization-independent metasurface implemented in this study (lens, self-accelerating beam generator, and hologram) consists of a square lattice of HfO_2 cylindrical nanopillars, where the diameter of each pillar varies as a function of its position within the lattice. Each nanopillar acts as a truncated dielectric waveguide with top and bottom interfaces of low reflectivity, through which light propagates with transmittance and phase shift controlled by the pillar height H, pillar diameter D, and lattice spacing P. For each targeted operation wavelength (λ_0 = 364 nm, 325 nm, and 266 nm), a corresponding pillar height (H = 550 nm, 500 nm, and 400 nm, respectively) and sub-wavelength lattice spacing (P = 200 nm, 190 nm, and 150 nm, respectively) are chosen, along with a range of pillar diameters that yield phase shifts varying over a full range of 2π, while maintaining a relatively high and constant transmittance ([50 nm, 160 nm], [50 nm, 150 nm], and [50 nm, 110 nm], respectively). The detailed design procedure is elaborated in Supplementary Information, Section VIII.

As a first demonstration of polarization-independent UV metasurfaces, two 500-μm-diameter, polarization-independent metalens designs, L_{364} and L_{325}, of identical numerical aperture NA = 0.6 (corresponding to focal length $f = 330$ μm), are implemented for focusing ultraviolet light at respective free-space wavelengths λ_0 = 364 nm and 325 nm (Fig. 2a). Singlet-mode focusing of a plane wave can be achieved by implementing the radially symmetric phase shift function $\varphi^L(x, y, \lambda_0) = mod\left((2\pi/\lambda_0)\ \left(f - \sqrt{x^2 + y^2 + f^2}\right), 2\pi\right)$, where f is the focal distance normal to the plane of the lens (along the *z* direction), *x* and *y* are in-plane distances along orthogonal directions from the center of the lens, and normal incidence is assumed. Each measured intensity distribution at the metalens focal plane (Supplementary Information, Section IX) reveals a circularly symmetric focal spot, characterized by a cross-section that closely matches the intensity distribution theoretically predicted for a diffraction-limited lens of numerical aperture NA = 0.6 and given by the Airy disk function $I(x) = [2J_1(A)/A]^2$, where J_1 is the Bessel function of the first kind of order one, and $A = 2\pi \mathrm{NA} x/\lambda_0$ (Figs. 2b and 2c). Metalens L_{325} exhibits a less-than-ideal focusing profile with larger side lobes, and this could be due to fabrication imperfections and nonideal realization of the required phase shift profile. The focusing efficiencies, defined as the ratio of the optical power of the focused spot to the total power illuminating the metalens, are (55.17 ± 2.56) % (L_{364}) and (56.28 ± 1.37) % (L_{325}). The cited uncertainties represent one standard deviation of the measured data.

Next, we demonstrate polarization-independent metasurfaces able to transform a normally-incident, plane wave into a diffraction-free output beam propagating along a curved trajectory, *i.e.*, a self-accelerating beam (SAB)[31-33]. Two 270-μm-square SAB generator designs, B_{364} and B_{325}, are implemented for operation at the respective wavelengths of 364 nm and 325 nm (Fig. 3a). SAB generator design and operation is conveniently described using a Cartesian coordinate system in which the constituent metasurface is located in the z = 0 plane and the 1st xy quadrant, with one corner positioned at the origin. The implemented SAB for each targeted free-space wavelength λ_0 = 364 nm and 325 nm, is characterized by a L-shaped wave-packet of main lobe centered on the trajectory $y = x = -az^2$, where $a = 9$ m^{-1} (in other words, originating from (0, 0, 0), propagating in the +z direction in a curved trajectory confined to the plane $y = x$, with a height above the surface given by $z = \sqrt{d/a}$, where $d = |x| = |y|$ is the lateral displacement). The targeted SAB can be generated by implementing a phase-shift profile $\varphi^B(x, y, \lambda_0) = mod\left(-\frac{8\pi}{3\lambda_0}\sqrt{a}\left(x^{\frac{3}{2}} + y^{\frac{3}{2}}\right), 2\pi\right)$ in the metasurface[34]. The measured lateral displacement values $d(z)$ are observed to closely match, in each case, the calculated values based on the targeted trajectory (Fig. 3b and Supplementary Information, Section X). The experimental SAB generated by each device exhibits diffraction-free characteristics with xy-plane intensity distributions similar to the intensity distributions numerically computed using the angular spectrum representation method[35], assuming an ideal metasurface realization having both the designed phase shift profile φ^B and unity transmittance T (Fig. 3c). The measured efficiencies, defined as the ratio of the total optical power of the SAB in the z = 5 mm plane to the total power illuminating the metasurface, are (46.75 ± 2.31) % (B_{364}) and (67.42 ± 4.43) % (B_{325}). The efficiencies compare favorably to that of a recently reported TiO_2-based self-accelerating beam generator operating at visible frequencies[36].

As a final demonstration of polarization-independent UV metasurfaces, we demonstrate three metaholograms, denoted H_{364}, H_{325}, and H_{266}, operating at three respective UV wavelengths λ_0 = 364 nm, 325 nm, and 266 nm (Fig. 4a). Implementing computer-generated holograms with metasurfaces has advantages including high efficiency, fine spatial resolution, low noise, compact footprint, and multiplexing capability[37-40]. Each demonstrated metahologram, which occupies a square area of side length 270 µm, is mapped to a Cartesian coordinate system in which the constituent metasurface is located in the z = 0 plane and the 1st xy quadrant, with one corner positioned at the origin. The Gerchberg-Saxton algorithm[41] is employed to calculate the required phase shift profile $\varphi_{364}^{H}(x,y,\lambda_0)$, $\varphi_{325}^{H}(x,y,\lambda_0)$, and $\varphi_{266}^{H}(x,y,\lambda_0)$ for producing a holographic "NIST" image located in the z = 40 mm plane, under normal-incidence, plane-wave illumination (Supplementary Information, Section XI). An additional offset of $y = -3$ mm is added to avoid overlap of the generated holographic image with the residual directly transmitted beam. The images projected by metaholograms H_{364}, H_{325}, and H_{266} are measured (Supplementary Information, Sections XII and XIII) and displayed in Fig. 4b, right panel. Each of the experimental holographic images faithfully replicates the shape of the corresponding target image (Fig. 4b, left panel), numerically computed assuming an ideal metahologram realization having both the designed phase shift profile φ^H for a given operation wavelength and unity transmittance T. In addition, the speckle patterns filling the shapes of the measured images projected by metaholograms H_{364} and H_{325} present numerous similarities to those of the corresponding target images; the as-measured holographic image projected by metahologram H_{266} does not offer the possibility of such a comparison due to the employed fluorescence transduction characterization scheme, which washes out the details of the speckle patterns. The measured efficiencies for metaholograms H_{364} and H_{325}, defined as the ratio of the total optical power of the holographic image to the total power illuminating the structure, are (62.99 ± 4.14) % and (71.78 ± 2.06) %, respectively. The measured efficiency for metahologram H_{266}, defined as the ratio of the total fluorescence power of the holographic image to the fluorescence power of light illuminating the structure (Supplementary Information, Section XIII), is (60.67 ± 2.60) %. These efficiency values are comparable to those of recently reported TiO_2-based metaholograms operating in the visible[26].

Spin-multiplexed ultraviolet metasurfaces. Metasurfaces have been demonstrated to switch between distinct optical outputs, such as different holographic images, or differently oriented beams, under the control of fundamental optical state of the input beam, such as polarization[42, 43], or a spatial feature of the input beam, such as angle of incidence[44]. Here, we demonstrate, for the first time, spin-multiplexed UV metasurfaces able to switch between distinct outputs depending on the handedness of input light (left-hand circularly polarized-LCP or right-hand circularly polarized-RCP). The detailed design procedure is elaborated in Supplementary Information, Section XIV.

As a first demonstration of a polarization-dependent, spin-multiplexed UV metasurface, we implement a self-accelerating beam generator operating at λ_0 = 364 nm, denoted $\mathrm{B}_{364}^{\mathrm{spin}}$, that generates SABs following different trajectories under the control of the handedness of circularly-polarized incident light. The spin-multiplexed SAB generator, which occupies a square area of side length l = 330 µm, is referenced to a Cartesian coordinate system in which the constituent metasurface is located in the z = 0 plane and the 1st xy quadrant, with one corner positioned at the origin. Two distinct phase shift profiles, $\varphi^{LCP}(x, y, \lambda_0) = mod\left(-\frac{8\pi}{3\lambda_0}\sqrt{16}\left(x^{\frac{3}{2}} + y^{\frac{3}{2}}\right), 2\pi\right)$ and $\varphi^{RCP}(x, y, \lambda_0) = mod\left(-\frac{8\pi}{3\lambda_0}\sqrt{2.25}\left((l-x)^{\frac{3}{2}} + (l-y)^{\frac{3}{2}}\right), 2\pi\right)$, are targeted for device operation, in order to yield SABs exiting the metasurface from opposite corners and following different trajectories, $y = x = -d_1 = -16z^2$, and $(y - l) = (x - l) = d_2 = 2.25z^2$, under LCP and RCP illumination, respectively (Figs. 5a and 5d). The measured lateral displacement values, $d_1(z)$ and $d_2(z)$, are observed to closely match, in each case, the calculated values based on the targeted trajectory (Figs. 5c and 5d). The experimental SAB generated by the device exhibits diffraction-free characteristics with xy-plane intensity distributions (Figs. 5e and 5f) similar to the targeted intensity distributions (Supplementary Information, Figs. S14 and S15), numerically computed assuming an ideal metasurface realization having both the designed phase shift profile φ^{LCP} (φ^{RCP}) and unity transmittance T. The measured efficiency under LCP (RCP illumination), defined as the ratio of the total optical power of the SAB in the z = 4.5 mm [z = 10.5 mm] plane to the total power illuminating the metasurface, is (38.42 ± 1.95) % [(61.90 ± 2.03) %]. The reduced efficiency under LCP illumination, compared to the RCP case, can be attributed to challenges associated with implementing a phase shift profile of higher spatial gradient (Supplementary Information, Section XVI).

Next, we demonstrate a spin-controlled metahologram operating at the same near-UV wavelength of 364 nm. The 330-µm-square metahologram, $\mathrm{H}_{364}^{\mathrm{spin}}$, located in the z = 0 plane, is designed to project a holographic "NIST" image (for LCP illuminating light) and "NJU" image (for RCP illuminating light) at λ_0 = 364 nm, all located in the xy-plane at z = 40 mm, with an offset of y = -3 mm (Fig. 6a; Corresponding phase shift profiles are plotted in Supplementary Information, Fig. S17). Both experimentally captured holographic images (Fig. 6b) faithfully replicate the shape of the corresponding targeted image computed from the designed phase profiles, including some fine grain details (Supplementary Information, Fig. S18). The measured efficiencies, defined as the ratio of the total optical power of the holographic image to the total power illuminating the metahologram, are (54.02 ± 2.22) % (under LCP illumination) and (53.76 ± 2.42) % (under RCP illumination), respectively.

Finally, a spin-multiplexed metahologram, $\mathrm{H}_{266}^{\mathrm{spin}}$, occupying a square area of side length of 320 μm, is implemented for operation at the deep-UV wavelength of 266 nm. The device, located in the z = 0 plane, is designed to project, at λ_0 = 266 nm, a holographic "deep" image for LCP illumination and a holographic "UV" image for RCP illumination, where both images are located in the z = 40 mm plane with a lateral offset of $y = -3$ mm (Fig. 6c; Corresponding phase shift profiles are plotted in Supplementary Information, Fig. S19). Each of the experimental holographic images (Fig. 6d) faithfully replicate the shape of the corresponding target image (Supplementary Information, Fig. S20), including subtle details of the chosen font, such as linewidth variation and serif. The measured efficiencies, defined as the ratio of the total fluorescence power of the holographic image to the fluorescence power of light illuminating the structure, are (58.95 ± 1.95) % under LCP illumination, and (61.23 ± 1.49) % under RCP illumination.

Discussion

Given the negligible extinction coefficient of the low-temperature-ALD deposited HfO_2 down to its bandgap ($\lambda_0 \approx 217$ nm), and the high patterning fidelity of the Damascene process, it should be straightforward to push the metasurface operation wavelengths to significantly shorter values than demonstrated here. In addition, experimental demonstration of broader range of device functionalities in the deep-UV regime other than hologram projection should be possible by using a continuous-wave light source and an appropriate direct imaging system. Moreover, the efficiency of HfO_2-based metasurface devices can be improved by further optimizing the Damascene process, or by employing advanced metasurface design strategies such as topology optimization[45] and generalized Huygens principle[46,47].

To conclude, an assortment of high-performance metasurface components operating in the ultraviolet regime, including down to the record-short deep-UV wavelengths, is demonstrated by using HfO_2, a CMOS-compatible, wide-bandgap, low-loss dielectric material, and an associated fabrication process based on low-temperature atomic layer deposition and Damascene lithography. This approach paves the way towards further development of “flat” UV optical elements having customized functionalities, as well as their integration into chip-scale nanophotonic systems, enabling applications such as atom trapping, fluorescence imaging, and circular dichroism spectroscopy in a compact form factor.

Materials and methods

Metasurface fabrication process. As the first step in the metasurface fabrication process, 500-µm-thick, double-side-polished UV-grade fused silica wafers are vapor-coated (150 °C) with an adhesion-enhancing monolayer of hexamethyldisilizane (HMDS). A layer of ZEP 520A resist is spin-coated onto the substrate, followed by baking on a hot plate at 180 °C for 10 minutes. The spin speed is adjusted to yield a resist thickness varying between 400 nm and 550 nm (as characterized by spectroscopic ellipsometry), depending on the specific metasurface design. To suppress charging during the electron beam (e-beam) lithography, a 20-nm-thick Al layer is thermally evaporated onto the ZEP layer (deposition rate: 0.1 nm/s). The ZEP-resist template is fabricated using e-beam lithography (accelerating voltage: 100 kV; beam current: 0.2 nA), followed by Al layer removal (AZ 400K 1:3 developer: 2 minutes; DI water: 1 minute) and resist development (hexyl acetate: 2 minutes; isopropyl alcohol: 30 seconds). Deposition of HfO_2 (deposition rate: 0.11 nm/cycle) is then performed using the low-temperature ALD described below. For all processed structures, the deposition thickness is chosen to be 200 nm, which not only exceeds the largest radius (or the largest semi-minor axis length) of the circular (or elliptical) openings of the exposed resist patterns for all metasurface designs -- providing complete filling of the patterns, but also provides a substantial over-coating of the resist -- yielding a quasi-planar top surface (Supplementary Information, Section VI). Following ALD, the HfO_2 layer is back-etched to the resist top surface using argon (Ar) ion milling (HfO_2 mill rate: ≈ 0.4 nm/s). During the Ar ion milling, a non-patterned, planar HfO_2 sample of the same initial thickness is back-etched at the same time, and its film thickness is measured by spectroscopic ellipsometry during breaks between etch segments of the entire ion milling process, to make sure that a proper milling time is employed. Finally, the remaining resist is removed by soaking in a solvent, yielding circular or elliptical HfO_2 posts with smooth and straight side-wall profiles (thanks to the resist templating process), of height varying from 400 nm to 550 nm (depending on the specific metasurface), and aspect ratios varying from ≈ 3 to ≈ 11.

Low-temperature TDMAH-based HfO_2 ALD. In step 1 of the ALD cycle, TDMAH vapor ($Hf[(CH_3)_2N]_4$) is pulsed into the ALD chamber for a duration t_1 = 1 s, reacting with the dangling O-H bonds on the hafnium-coated surface to create a new solid monolayer of $Hf[(CH_3)_2N]_2O$, and generate the gas by-product $(CH_3)_2NH$ (dimethylamine). In step 2, high-purity nitrogen (N_2) gas is flowed for a duration t_2 = 75 s to fully remove any un-reacted TDMAH vapor and dimethylamine byproduct from the chamber. In step 3, water vapor is pulsed into the chamber for a duration t_3 = 60 ms, reacting with the $Hf[(CH_3)_2N]_2O$ to create a monolayer of HfO_2 on the surface. Finally, in step 4, the excessive water vapor as well as the Dimethylamine reaction byproduct are completely removed from the chamber by N_2 purging for a duration t_4 = 75 s.

Data availability

The data that support the plots within this paper and other finding of this study are available from the corresponding authors upon request.

Acknowledgements

Q. F., Y. L., and T. X. acknowledge the support by national key R&D program of China (Grant # 2017YFA0303700 and 2016YFA0202100), and National Science Foundation of China (Grant # 11774163). C. Z., S. D., W. Z. and A. A. acknowledge support under the Cooperative Research Agreement between the University of Maryland and the National Institute of Standards and

Technology Physical Measurement Laboratory, Award # 70NANB14H209, through the University of Maryland. C. Z acknowledges the start-up funding from Huazhong University of Science and Technology, and helpful discussions with Dr. Huazhi Li.

Certain commercial equipment and software are identified in this documentation to describe the subject adequately. Such identification does not imply recommendation or endorsement by the NIST, nor does it imply that the equipment identified is necessarily the best available for the purpose.

Conflict of interest

The authors declare no competing interests.

Author contributions

The project was initiated by C. Z. The device fabrication and characterization were performed by C. Z., S. D., W. Z. and A. A. Simulations were performed by Q. F., S. D., C. Z. with further analysis by Y. L., T. X. and H. J. L. All authors contributed to the interpretation of results and participated in manuscript preparation.

References

1. Yu, N. & Capasso, F. Flat optics with designer metasurfaces. *Nat. Mater.* **13**, 139-150 (2014).

2. Hsiao, H. H., Chu, C. H. & Tsai, D. P. Fundamentals and applications of metasurfaces. *Small Methods* **1**, 1600064 (2017).

3. Kildishev, A. V., Boltasseva, A. & Shalaev, V. M. Planar photonics with metasurfaces. *Science* **339**, 1232009 (2013).

4. Ding, F., Pors, A. & Bozhevolnyi, S. I. Gradient metasurfaces: a review of fundamentals and applications. *Rep. Prog. Phys.* **81**, 026401 (2017).

5. Chen, H. T., Taylor, A. J. & Yu, N. A review of metasurfaces: physics and applications. *Rep. Prog. Phys.* **79**, 076401 (2016).

6. Kamali, S. M., Arbabi, E., Arbabi, A. & Faraon, A. A review of dielectric optical metasurfaces for wavefront control. *Nanophotonics* **7**, 1041-1068 (2018).

7. Zhang, L., Mei, S., Huang, K. & Qiu, C. W. Advances in full control of electromagnetic waves with metasurfaces. *Adv. Opt. Mater*. **4**, 818-833 (2016).

8. Sun, S., He, Q., Hao, J., Xiao, S. & Zhou, L. Electromagnetic metasurfaces: physics and applications. *Adv. Opt. Photon.* **11**, 380-479 (2019).

9. Luo, X. Subwavelength optical engineering with metasurface waves. *Adv. Opt. Mater*. **6**, 1701201 (2018).

10. Arbabi, A., Horie, Y., Bagheri, M. & Faraon, A. Dielectric metasurfaces for complete control of phase and polarization with subwavelength spatial resolution and high transmission. *Nature Nanotechnol.* **10**, 937-943 (2015).

11. Lin, D., Fan, P., Hasman, E. & Brongersma, M. L. Dielectric gradient metasurface optical elements. *Science* **345**, 298-302 (2014).

12. Divitt, S., Zhu, W., Zhang, C., Lezec, H. J. & Agrawal, A. Ultrafast optical pulse shaping using dielectric metasurfaces. *Science* **364**, 890-894 (2019).

13. Khorasaninejad, M. et al. Metalenses at visible wavelengths: diffraction-limited focusing and subwavelength resolution imaging. *Science* **352**, 1190-1194 (2016).

14. Chen, W. T. et al. A broadband achromatic metalens for focusing and imaging in the visible. *Nat. Nanotechnol.* **13**, 220-226 (2018).

15. Wang, S. et al. A broadband achromatic metalens in the visible. *Nature Nanotechnol.* **13**, 227-232 (2018).

16. Ren, H. et al. Metasurface orbital angular momentum holography. *Nat. Commun.* **10**, 2986 (2019).

17. Day, R. N. & Davidson, M. W. The fluorescent protein palette: tools for cellular imaging. *Chem. Soc. Rev*. **38**, 2887 (2009).

18. Greenfield, N. J. Using circular dichroism spectra to estimate protein secondary structure. *Nat. Protoc.* **1**, 2876-2890 (2006).

19. Ludlow, A. D., Boyd, M. M., Ye, J., Peik, E. & Schmidt, P. O. Optical atomic clocks. *Rev. Mod. Phys.* **87**, 637 (2015).

20. Huang, K. et al. Ultraviolet metasurfaces of $\approx 80\%$ efficiency with antiferromagnetic resonances for optical vectorial anti-counterfeiting. *Laser Photonics Rev.* **13**, 1800289 (2019).

21. Deng, Y. et al. All-silicon broadband ultraviolet metasurfaces. *Adv. Mater.* **30**, 1802632 (2018).

22. Robertson, J. High dielectric constant oxides. Eur. Phys. J. Appl. Phys. *28*, 265-291 (2004).

23. Wilk, G. D., Wallace, R. M. & Anthony, J. M. High-κ gate dielectrics: current status and materials properties considerations. *J. Appl. Phys.* **89**, 5243 (2001).

24. Andricacos, P. C., Uzoh, C., Dukovic, J. O., Horkans, J. & Deligianni, H. Damascene copper electroplating for chip interconnections. *IBM J. Res. Dev.* **42**, 567-574 (1998).

25. Schmid, G. M. et al. Implementation of an imprint damascene process for interconnect fabrication. *J. Vac. Sci. Technol. B Nanotechnol. Microelectron.* **24**, 1283-1291 (2006).

26. Devlin, R. C., Khorasaninejad, M., Chen, W. T., Oh, J. & Capasso, F. Broadband high-efficiency dielectric metasurfaces for the visible spectrum. *Proc. Natl. Acad. Sci. U.S.A.* **113**, 10473-10478 (2016).

27. Lowalekar, V. & Raghavan, S. Etching of zirconium oxide, hafnium oxide, and hafnium silicates in dilute hydrofluoric acid solutions. *J. Mater. Res.* **19**, 1149-1156 (2011).

28. Liu, X. et al. ALD of hafnium oxide thin films from Tetrakis(ethylmethylamino)hafnium and ozone. *J. Electrochem. Soc.* **152**, G213-F219 (2005).

29. Kukli, K., Ritala, M., Sajavaara, T., Keinonen, J. & Leskelä, M. Comparison of hafnium oxide films grown by atomic layer deposition from iodide and chloride precursors. *Thin Solid Films* **416**, 72-79 (2002).

30. Hausmann, D. M., Kim, E., Becker, J. & Gordon, R. G. Atomic layer deposition of hafnium and zirconium oxides using metal amide precursors. *Chem. Mater.* **14**, 4350-4358 (2002).

31. Siviloglou, G. A., Broky, J., Dogariu, A. & Christodoulides, D. N. Observation of accelerating Airy beams. *Phys. Rev. Lett*. **99**, 213901 (2007).

32. Siviloglou, G. A. & Christodoulides, D. N. Accelerating finite energy Airy beams. *Opt. Lett.* **32**, 979-981 (2007).

33. Henstridge, M. et al. Accelerating light with metasurfaces. *Optica* **5**, 678-681 (2018).

34. Cottrell, D. M., Davis, J. A. & Hazard, T. M. Direct generation of accelerating Airy beams using a 3/2 phase-only pattern. *Opt. Lett.* **34**, 2634-2636 (2009).

35. Novotny, L. & Hecht, B. Principles of Nano-Optics Ch. 3 (Cambridge Univ. Press, Cambridge, 2006).

36. Fan, Q. et al. Broadband generation of photonic spin-controlled arbitrary accelerating light beams in the visible. *Nano Lett*. **19**, 1158-1165 (2019).

37. Wang, L. et al. Grayscale transparent metasurface holograms. *Optica* **3**, 1504-1505 (2016).

38. Wang, B. et al. Polarization-controlled color-tunable holograms with dielectric metasurfaces. *Optica* **4**, 1368-1371 (2017).

39. Yue, Z., Xue, G., Liu, J., Wang, Y. & Gu, M. Nanometric holograms based on a topological insulator material. *Nat. Commun.* **8**, 15354 (2017).

40. Huang, L., Zhang, S. & Zentgraf, T. Metasurface holography: from fundamentals to applications. *Nanophotonics* **7**, 1169-1190 (2018).

41. Gerchberg, R. W. & Saxton, W. O. A practical algorithm for the determination of the phase from image and diffraction plane pictures. *Optik* **35**, 237-246 (1972).

42. Balthasar, M. J. P., Rubin, N. A., Devlin, R. C., Groever, B. & Capasso, F. Metasurface polarization optics: independent phase control of arbitrary orthogonal states of polarization. *Phys. Rev. Lett.* **118**, 113901 (2017).

43. Wang, K. et al. Quantum metasurface for multiphoton interference and state reconstruction. *Science* **361**, 1104-1108 (2018).

44. Kamali, S. M. et al. Angle-multiplexed metasurfaces: encoding independent wavefronts in a single metasurface under different illumination angles. *Phys. Rev. X* **7**, 041056 (2017).

45. Phan, T. et al. High-efficiency, large-area, topology-optimized metasurfaces. *Light Sci. Appl.* **8**, 48 (2019).

46. Decker, M. et al. High-efficiency dielectric Huygens' surfaces. *Adv. Opt. Mater.* **3**, 813-820 (2015).

47. Pfeiffer, C. & Grbic, A. Metamaterial Huygens' surfaces: Tailoring wave fronts with reflectionless sheets. *Phys. Rev. Lett.* **110**, 197401 (2013)

Figure Captions

Fig. 1 | Implementation of ultraviolet metasurfaces. a, Schematic representation of a metasurface unit cell, consisting of a high-aspect-ratio HfO_2 pillar of height H, elliptical cross-section (principle axis lengths D_1 and D_2), and rotation angle θ, arranged on a SiO_2 substrate to form a square lattice with sub-wavelength lattice spacing P. Specific optical functions are implemented via the variation of D_1, D_2, and θ as a function of nanopillar position within the lattice. **b**, Schematic representation of the developed low-temperature ALD cycle using TDMAH precursor, H_2O reactant, and process temperature T_p = 95 °C. **c,** Refractive index n and extinction coefficient k of as-deposited HfO_2 film, measured using spectroscopic ellipsometry. Values of n at the three operation wavelengths targeted in this study are denoted by yellow stars. Dashed line indicates position of HfO_2 bandgap E_g. **d,** Scanning electron micrograph (SEM) of details of a fabricated polarization-independent metalens designed for operation at λ_0 = 325 nm, showing a lattice of 500-nm tall, circularly-shaped HfO_2 nanopillars of varying diameters. Viewing angle: 52°. **e,** SEM of details of a fabricated spin-multiplexed metahologram designed for operation at λ_0 = 266 nm, showing a lattice of 480-nm tall, elliptically-shaped HfO_2 nanopillars of varying in-plane cross-sections and rotation angles. Viewing angle: 52°. The nanopillars are coated with a layer of Au / Pd alloy (≈ 5 nm thick) to suppress charging during imaging. **f,** Optical micrographs of full metalens (top panel) and spin-multiplexed metahologram (bottom panel), corresponding respectively, to metasurfaces described in **d** and **e**. Scale bars: 100 µm.

Fig. 2 | Polarization-independent near-UV metalenses. a, Schematic representation of focusing by metalens, L_{364} or L_{325}, under normal-incidence, plane-wave illumination at λ_0 = 364 nm or 325 nm, respectively. **b, c,** Cross-focus cuts and intensity distributions in the focal plane, as measured for metalens L_{364} and L_{325}, respectively. Theoretically predicted cross-focus cuts are plotted for reference. Scale bars: 1 µm.

Fig. 3 | Polarization-independent near-UV self-accelerating beam generators. a, Schematic representation of the generation of a self-accelerating beam by metasurface, B_{364} or B_{325}, under normal-incidence, plane-wave illumination at λ_0 = 364 nm or 325 nm, respectively. **b,** Measured transverse defection in different *z* planes (ranging from 2.5 mm to 5.5 mm, with an increment of 0.5 mm) for illumination of B_{364} and B_{325}, respectively, at respective operation wavelengths λ_0 = 364 nm and 325 nm. Error bars denote one standard deviation of the measured data. The targeted beam trajectory, $d = 9z^2$, is shown for reference. **c,** Measured and computed *xy*-plane intensity distributions (normalized) at different *z* planes for both devices at their designated wavelengths of operation. Each distribution is displayed over an equal square area of side length 120 µm, but shifted along the $-xy$ direction as a function of increasing *z*, such that the center of the main lobe maintains an invariant position within each image.

Fig. 4 | Polarization-independent near- and deep-UV metaholograms. a, Schematic representation of the holographic image projection by metahologram, H_{364}, H_{325}, or H_{266}, under normal-incidence, plane-wave illumination at λ_0 = 364 nm, 325 nm, or 266 nm, respectively. **b,** Targeted (left panel) and measured (right panel) holographic images projected by the metaholograms H_{364}, H_{325}, and H_{266} in the *z* = 40 mm plane.

Fig. 5 | Spin-multiplexed near-UV self-accelerating beam generator. a, b, Schematic representation of the generation of a self-accelerating beam by the spin-multiplexed metasurface, $\mathrm{B}_{364}^{\mathrm{spin}}$, under normal-incidence, plane-wave LCP (**a**) or RCP (**b**) illumination at λ_0 = 364 nm. **c,** Measured transverse defection in different *z* planes (ranging from 2.5 mm to 4.5 mm, with an increment of 0.5 mm) for LCP illumination of $\mathrm{B}_{364}^{\mathrm{spin}}$ at its operation wavelength λ_0 = 364 nm. Error bars denote one standard deviation of the measured data. The targeted beam trajectory, $d = 16z^2$, is shown for reference. **d,** Measured transverse defection in different z planes (ranging from 4.5 mm to 10.5 mm, with an increment of 1.5 mm) for RCP illumination of $\mathrm{B}_{364}^{\mathrm{spin}}$ at its operation wavelength λ_0 = 364 nm. Error bars denote one standard deviation of the measured data. The targeted beam trajectory, $d = 2.25z^2$, is shown for reference. **e, f,** Measured *xy*-plane intensity distributions (normalized) at different *z* planes for the device at its designated wavelength of operation under either LCP illumination (**e**) or RCP illumination (**f**). Each distribution is displayed over an equal square area of side length 140 μm, but shifted along the $-xy$ (**e**) or xy (**f**) direction as a function of increasing z, such that the center of the main lobe maintains an invariant position within each image.

Fig. 6 | Spin-multiplexed near- and deep-UV metaholograms. a, Schematic representation of the holographic image projection by the spin-multiplexed metahologram $\mathrm{H}_{364}^{\mathrm{spin}}$ under LCP or RCP illumination at λ_0 = 364 nm, respectively. **b,** Measured holographic images projected by metahologram $\mathrm{H}_{364}^{\mathrm{spin}}$ in the *z* = 40 mm plane under LCP illumination (top image) and RCP illumination (bottom image). **c,** Schematic representation of the holographic image projection by the spin-multiplexed metahologram $\mathrm{H}_{266}^{\mathrm{spin}}$ under LCP or RCP illumination at λ_0 = 266 nm, respectively. **d,** Measured holographic images projected by metahologram $\mathrm{H}_{266}^{\mathrm{spin}}$ in the *z* = 40 mm plane under LCP illumination (top image) and RCP illumination (bottom image).

Figure 1: Implementation of ultraviolet metasurfaces.

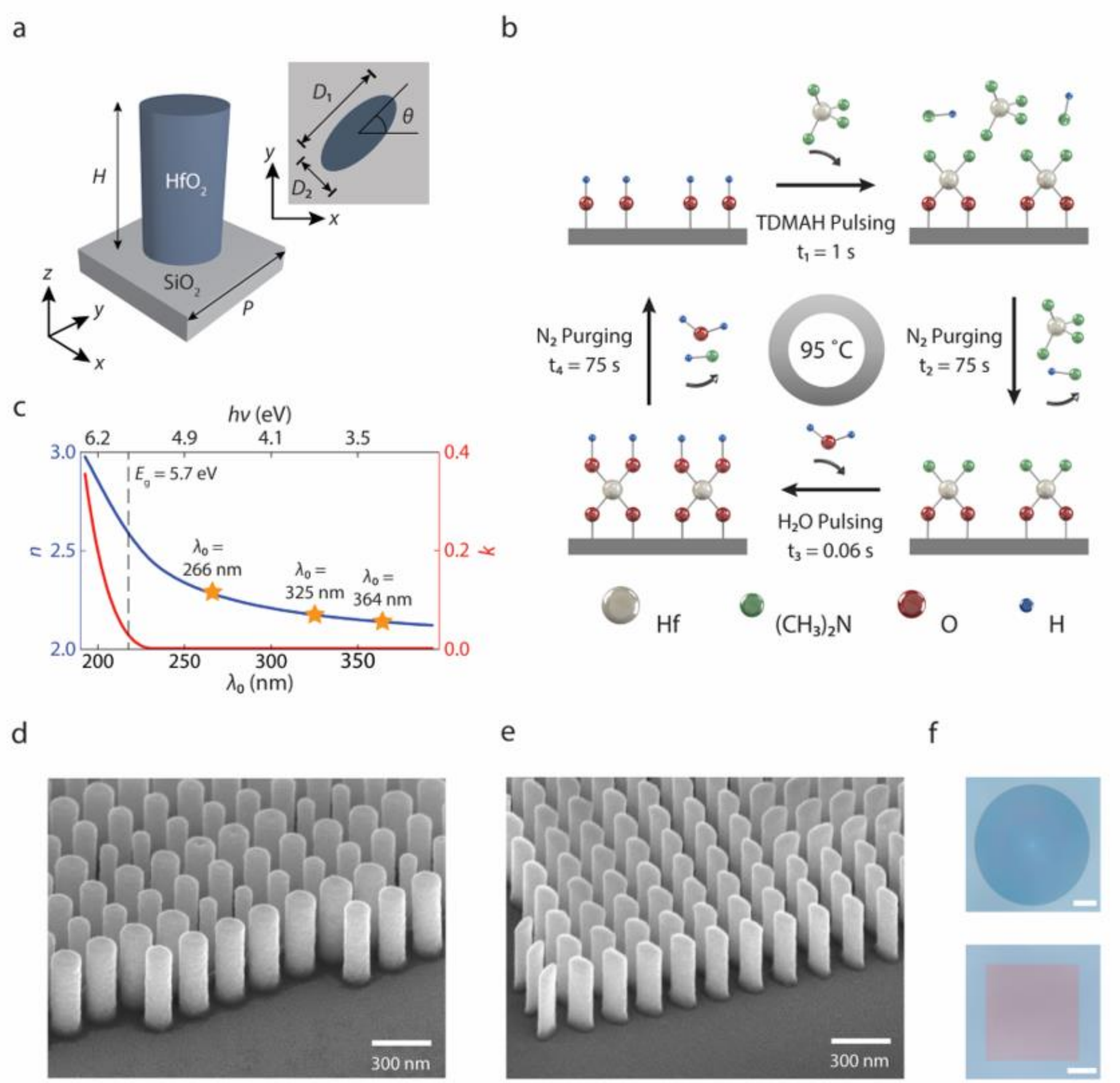

Figure 2: Polarization-independent near-UV metalenses.

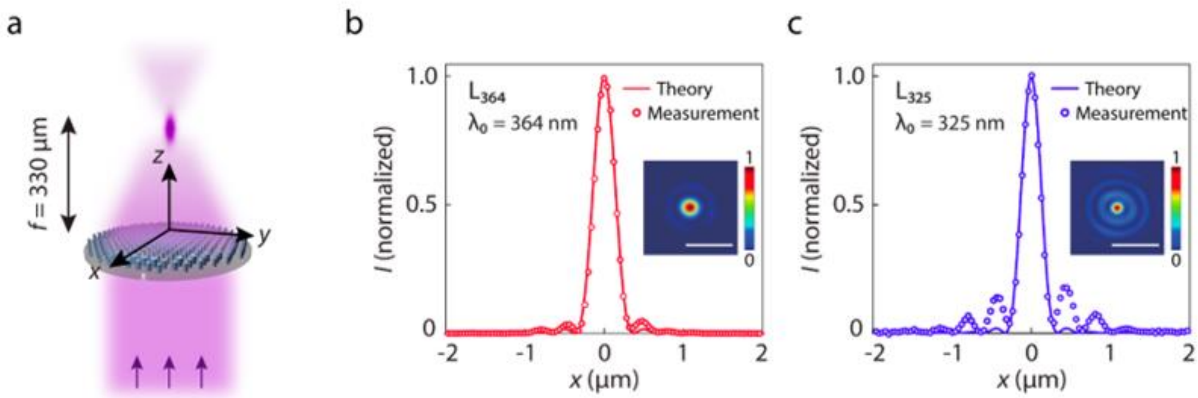

Figure 3: Polarization-independent near-UV self-accelerating beam generators.

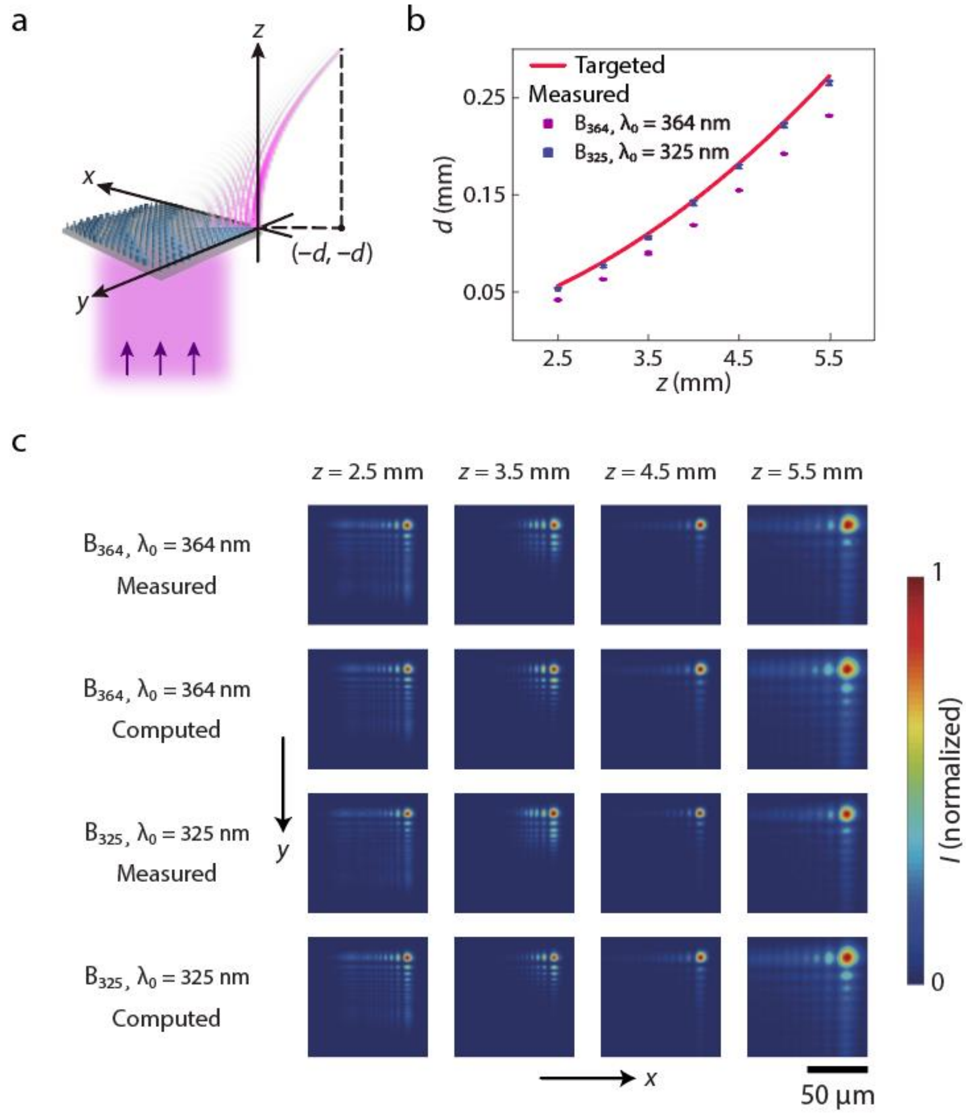

Figure 4: Polarization-independent near- and deep-UV metaholograms.

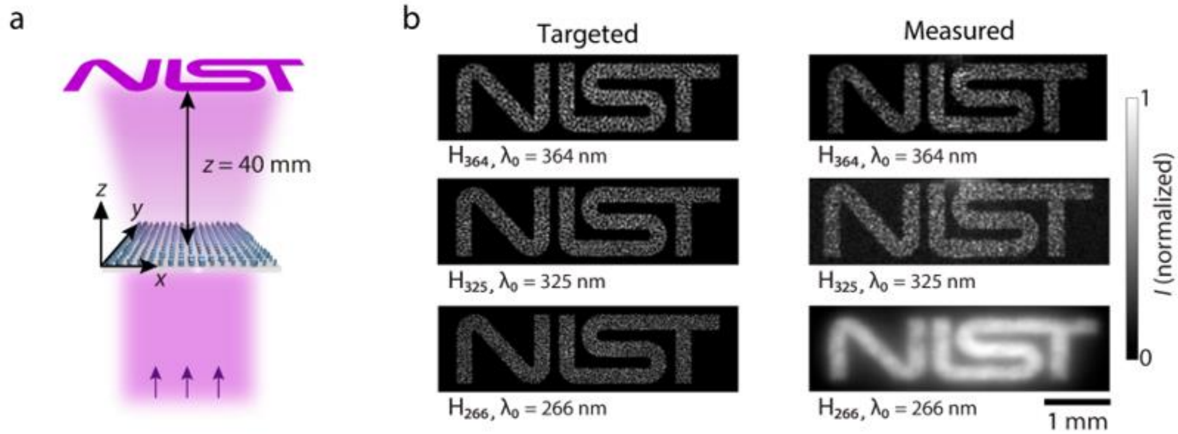

Figure 5: Spin-multiplexed near-UV self-accelerating beam generator.

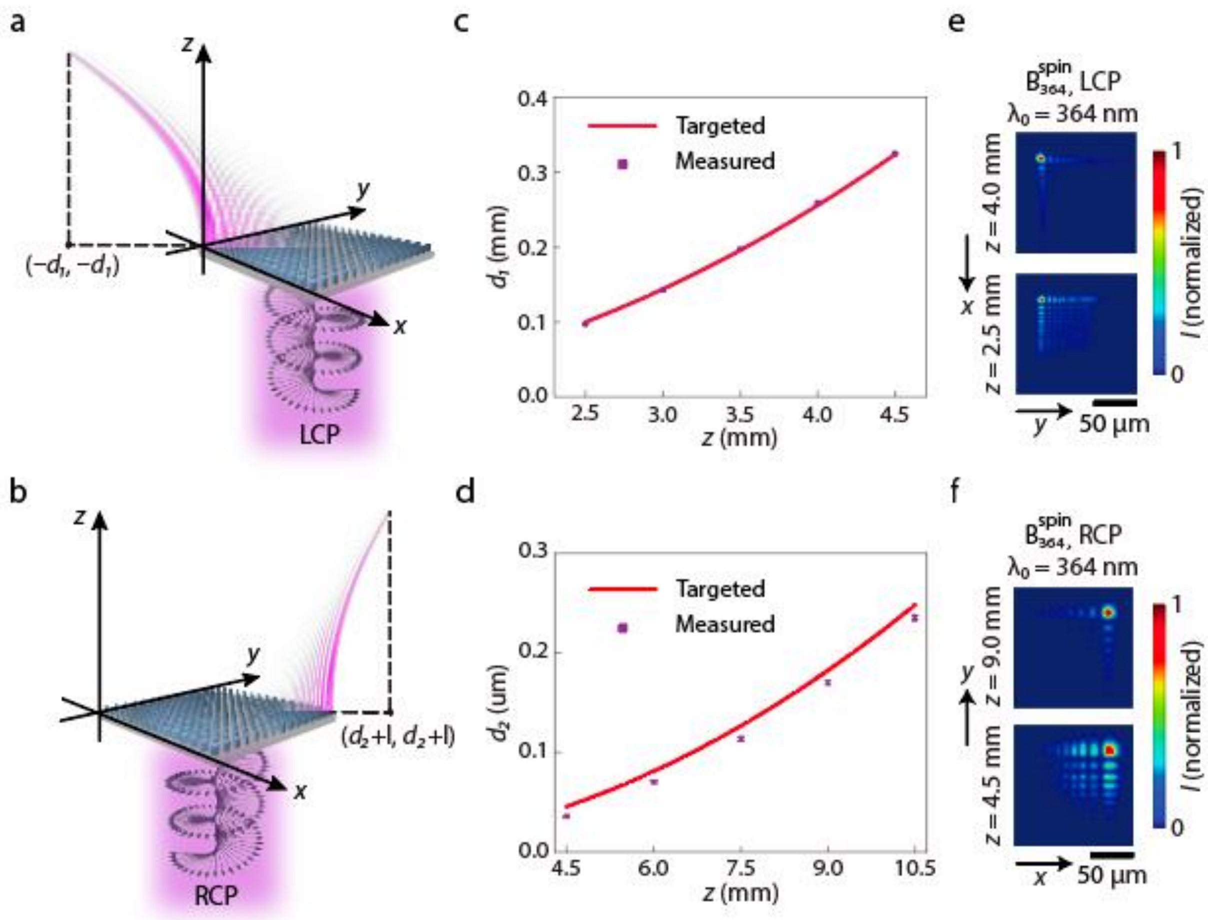

Figure 6: Spin-multiplexed near- and deep-UV metaholograms.

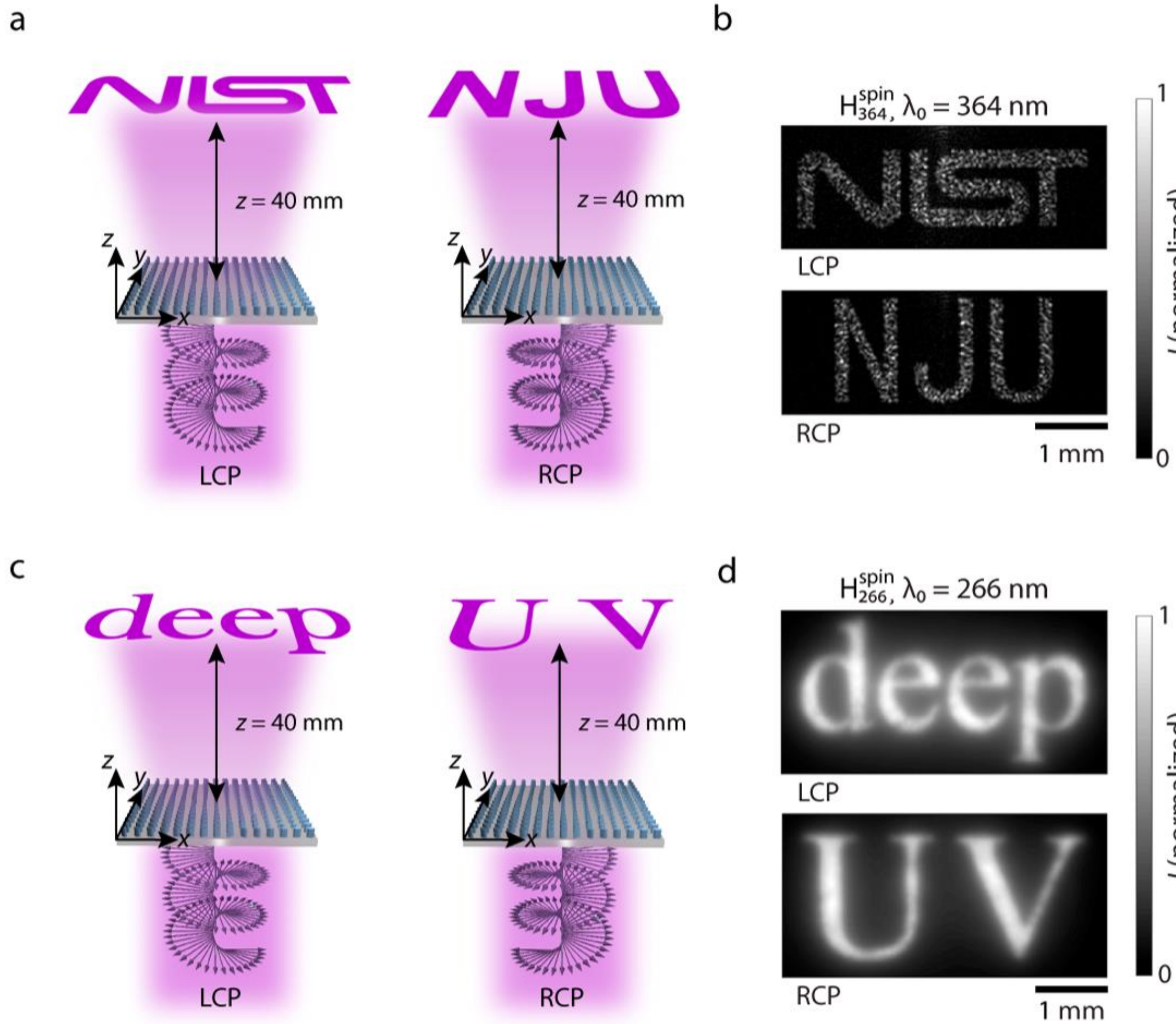

Supplementary Information for

Low-loss Metasurface Optics down to the Deep Ultraviolet Region

Cheng Zhang[1,2,3†,*], Shawn Divitt[2,3†], Qingbin Fan[4†], Wenqi Zhu[2,3], Amit Agrawal[2,3], Yanqing Lu[4], Ting Xu[4*] and Henri J. Lezec[2,*]

[1.] School of Optical and Electronic Information & Wuhan National Laboratory for Optoelectronics, Huazhong University of Science and Technology, Wuhan, 430074, China.

[2.] Physical Measurement Laboratory, National Institute of Standards and Technology, Gaithersburg, MD, 20899, USA.

[3.] Maryland Nanocenter, University of Maryland, College Park, MD, 20742, USA.

[4.] National Laboratory of Solid State Microstructures, College of Engineering and Applied Sciences and Collaborative Innovation Center of Advanced Microstructures, Nanjing University, Nanjing, 210093, China.

[†] Equal contributors

[*] Corresponding authors. Cheng Zhang, Email: cheng.zhang@hust.edu.cn; Ting Xu, Email: xuting@nju.edu.cn; Henri J. Lezec, Email: henri.lezec@nist.gov

This Supplementary Information includes:

Section I. Transmittance of the UV-grade fused silica substrate

Section II. X-ray diffraction (XRD) characterization of ALD-deposited HfO_2

Section III. Spectroscopic ellipsometry characterization of low-temperature ALD-deposited HfO_2

Section IV. Comparison of UV optical properties of ALD-deposited HfO_2 at 95 °C and 200 °C

Section V. Optical properties of ALD-deposited HfO_2 and TiO_2 over the UV and visible range

Section VI. Atomic force microscopy (AFM) characterization of the top surfaces of the patterned and non-patterned resist areas after the ALD coating

Section VII. Scanning electron micrographs of UV metasurfaces

Section VIII. Design of the polarization-independent metasurfaces

Section IX. Characterization procedure for metalenses L_{364} and L_{325}

Section X. Characterization procedure for self-accelerating beam generators B_{364} and B_{325}

Section XI. Designed phase shift profiles φ_{364}^{H}, φ_{325}^{H}, and φ_{266}^{H} for metaholograms H_{364}, H_{325}, and H_{266}

Section XII. Characterization procedure for metaholograms H_{364} and H_{325}

Section XIII. Characterization procedure for metahologram H_{266}

Section XIV. Design of spin-multiplexed metasurfaces

Section XV. Characterization procedure for spin-multiplexed self-accelerating beam generator $\mathrm{B}_{364}^{\mathrm{spin}}$

Section XVI. Discussion of reduced device efficiency under LCP illumination for $\mathrm{B}_{364}^{\mathrm{spin}}$

Section XVII. Implementation of spin-multiplexed metahologram $\mathrm{H}_{364}^{\mathrm{spin}}$

Section XVIII. Implementation of spin-multiplexed metahologram $\mathrm{H}_{266}^{\mathrm{spin}}$

I. Transmittance of the UV-grade fused silica substrate

As displayed in Fig. S1, the 500-µm-thick, UV-grade fused silica wafer utilized as metasurface substrate provides a high optical transmittance (> 90 %) over the wavelength range exploited in this study (266 nm to 364 nm).

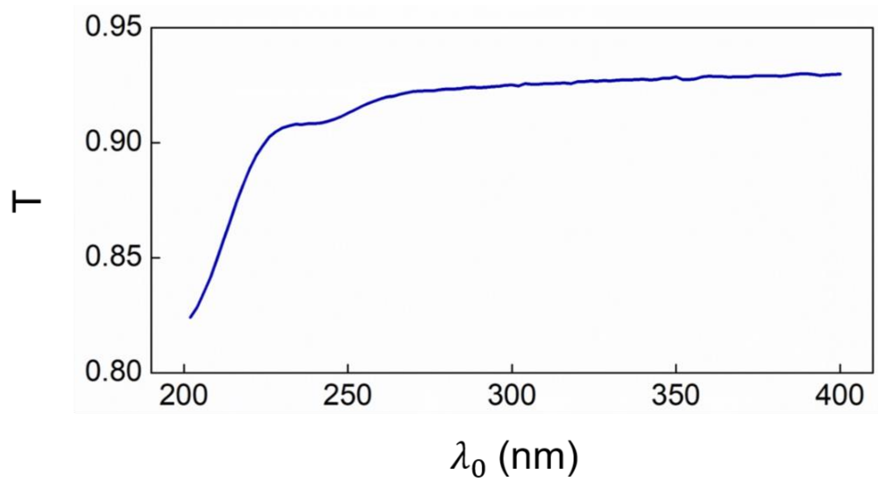

Fig. S1. Measured transmittance versus wavelength of a 500-µm-thick, UV-grade fused silica wafer.

II. X-ray diffraction (XRD) characterization of ALD-deposited HfO_2

Glancing angle x-ray diffraction (XRD) characterization is performed on a 200-nm-thick HfO_2 film grown by the low-temperature ALD on an amorphous UV-grade fused silica substrate, using a theta-2theta scan configuration. The angle of incidence is 0.7°, the scan range is from 30° to 120°, and the scan speed is set to 2°/min. The XRD angular spectrum (Fig. S2) reveals that the ALD-deposited HfO_2 is amorphous as evidenced by the absence of diffraction peaks.

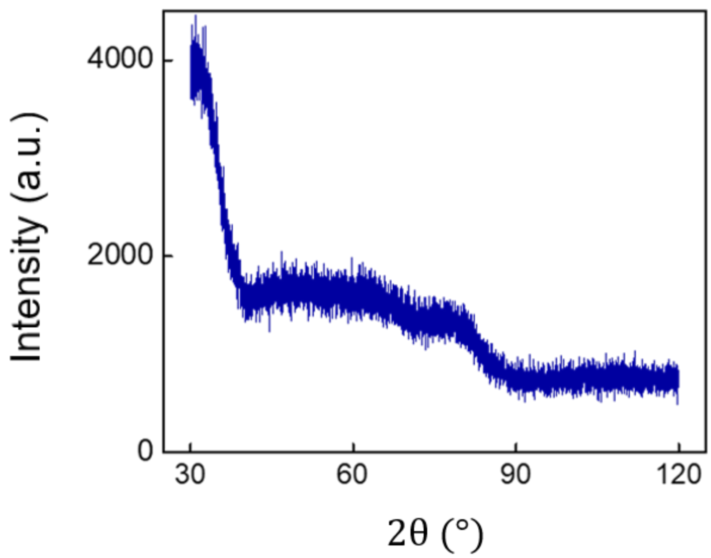

Fig. S2. X-ray diffraction (XRD) angular spectrum of ALD-deposited HfO_2.

III. Spectroscopic ellipsometry characterization of low-temperature ALD-deposited HfO_2

A 200-nm-thick HfO_2 film is grown by low-temperature ALD on a silicon wafer coated with a 300-nm-thick thermal oxide layer. The film's optical properties are characterized by reflection-mode spectroscopic ellipsometry using the interference enhancement method[1, 2], at three different angles of incidence (55°, 65°, and 75°) with respect to the normal to the plane of the HfO_2 layer. The dielectric function of the HfO_2 is modelled by a Tauc-Lorentz oscillator. The measured and best-match modeled Psi (Ψ) and Delta (Δ) curves (Fig. S3) display close correspondence, as evidenced by a low mean-squared-error for the fit (MSE = 6.686). The corresponding curves for the extracted values of refractive index n and extinction coefficient k are plotted in the main text (Fig. 1c).

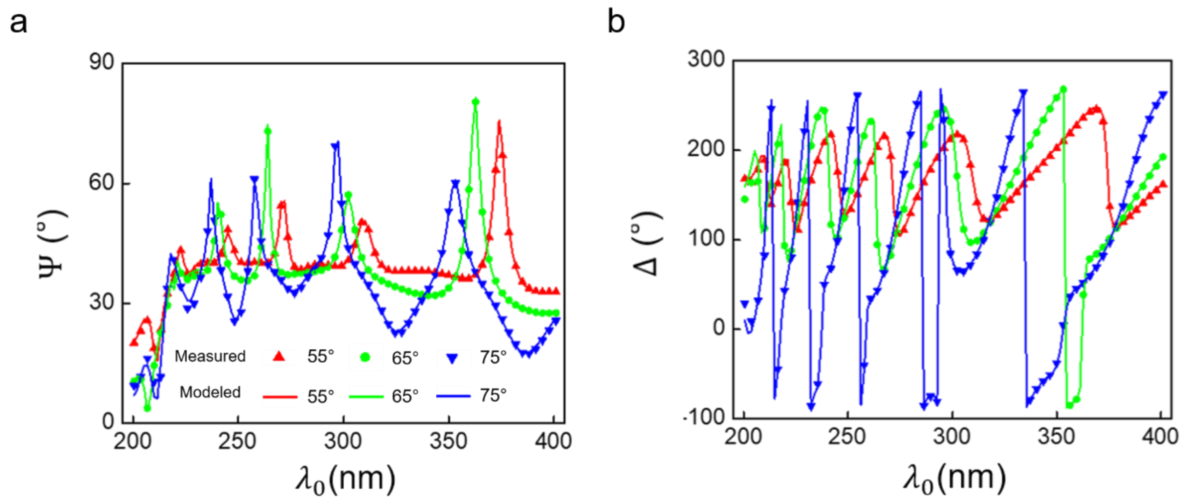

Fig. S3. Measured and best-match modeled Psi and Delta curves for ellipsometric characterization of low-temperature ALD-deposited HfO_2. The legend in Fig. S3a applies to Fig. S3b.

IV. Comparison of UV optical properties of ALD-deposited HfO_2 at 95 °C and 200 °C

The UV optical properties (characterized by spectroscopic ellipsometry) of HfO_2 deposited by TDMAH / water-based ALD using the new, low-temperature process (process temperature: T_p = 95 °C, TDMAH pulsing time: t_1 = 1 s, N_2 purging time: t_2 = 75 s, H_2O pulsing time: t_3 = 60 ms, N_2 purging time: t_4 = 75 s, and deposition rate: 0.110 nm/cycle) are compared to those resulting from deposition using a standard process (process temperature: T_p = 200 °C, TDMAH pulsing time: t_1 = 250 ms, N_2 purging time: t_2 = 12 s, H_2O pulsing time: t_3 = 60 ms, N_2 purging time: t_4 = 12 s, and deposition rate: 0.106 nm / cycle). Over the UV range, the two films exhibit (Fig. S4) virtually identical extinction coefficients k (where $k \approx 0$ for $\lambda_0 \geq 220$ nm), and refractive indices n that differ only slightly (where values for the film deposited at 95 °C are at most lower by ≈ 0.03 than those for film deposited at 200 °C, at any given wavelength in that range).

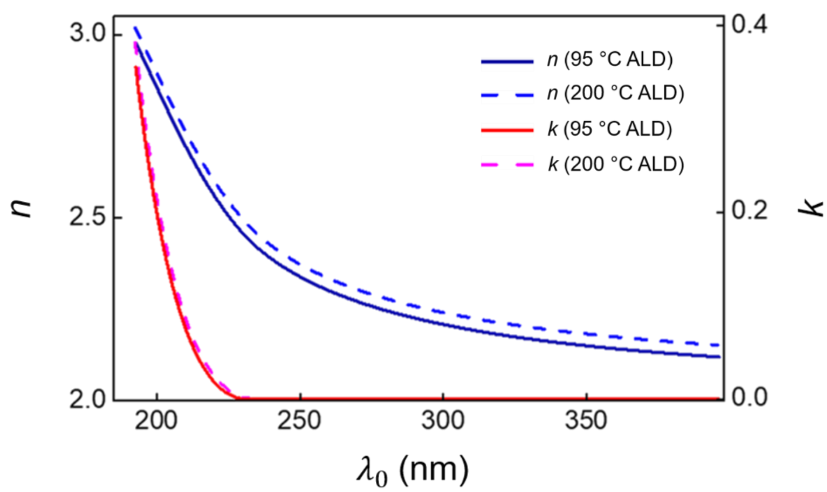

Fig. S4. Measured refractive index n and extinction coefficient k of HfO_2 films deposited by ALD at 95 °C and 200 °C, respectively.

V. Optical properties of ALD-deposited HfO_2 and TiO_2 over the UV and visible range

As displayed in Fig. S5, the 95°C-ALD-deposited HfO_2 film exhibits a high refractive index ($n >$ 2.0) and zero optical loss ($k = 0$) in the visible range (380 nm $\leq \lambda_0 \leq$ 800 nm), making it suitable for fabricating low-loss metasurface devices in this wavelength range as well. The optical constants of a more commonly used material in this spectral range, TiO_2, is also shown for comparison.

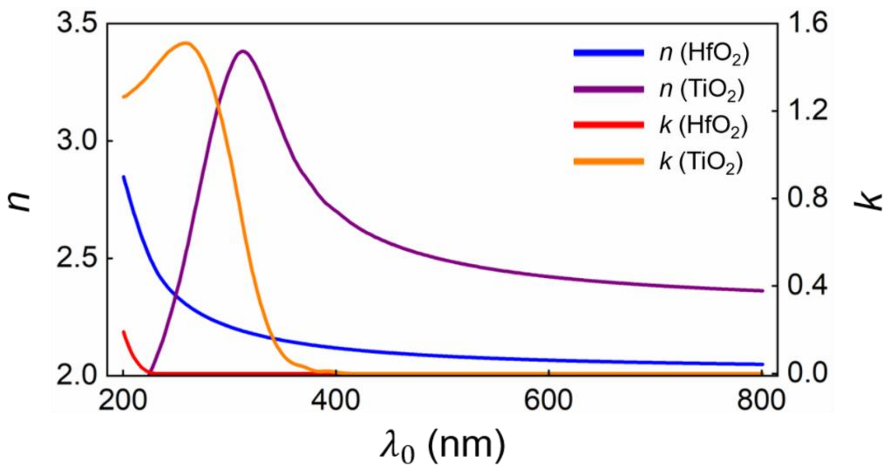

Fig. S5. Measured refractive index *n* and extinction coefficient *k* of the 95°C-ALD-deposited HfO_2 films and the 90°C-ALD-deposited TiO_2 films in the UV and visible range.

VI. Atomic force microscopy (AFM) characterization of the top surfaces of the patterned and non-patterned resist areas after the ALD coating

Atomic force microscopy (AFM) characterization is performed on the top surfaces of a patterned resist area (Fig. S6, Left) and a non-patterned resist area (Fig. S6, Right) after the 200-nm-thick HfO_2 ALD coating. Both the patterned and non-patterned areas exhibit similar quasi-planar surface morphologies with RMS roughness values of 4.32 nm and 4.13 nm, respectively.

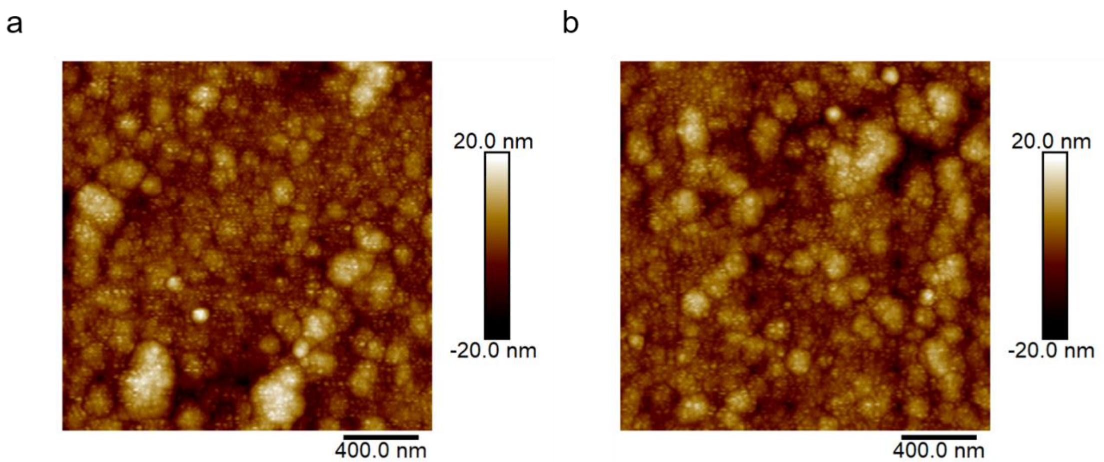

Fig. S6. Atomic force microscopy (AFM) characterization over the top surfaces of a patterned resist area (left) and non-patterned resist area (right) after the 200-nm-thick HfO_2 ALD coating. The scan is performed over a square area with side length of 2 µm.

VII. Scanning electron micrographs of UV metasurfaces

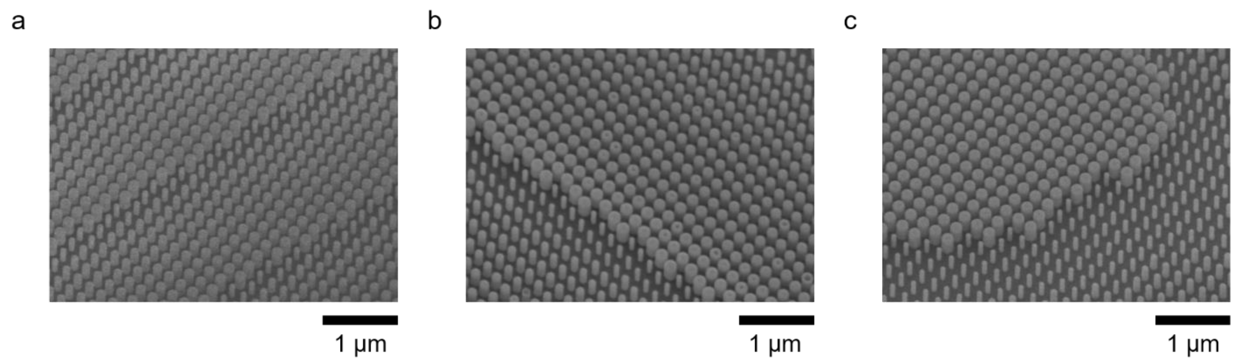

Fig. S7. Scanning electron micrographs (viewing angle: 20°) of selected areas of polarization-independent metasurfaces designed for operation at λ_0 = 364 nm. **a**, Metalens L_{364} . **b**, Self-accelerating beam generator B_{364}. **c**, Metahologram H_{364}.

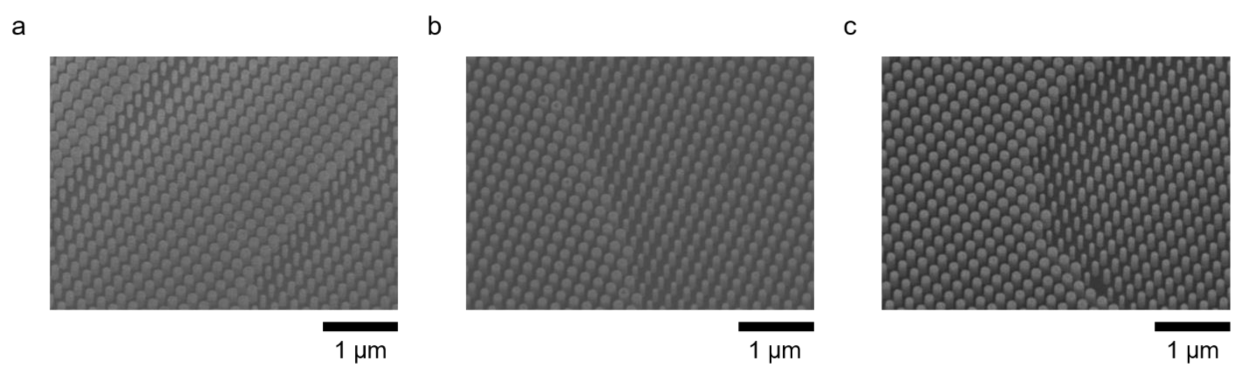

Fig. S8. Scanning electron micrographs (viewing angle: 20°) of selected areas of polarization-independent metasurfaces designed for operation at λ_0 = 325 nm. **a**, Metalens L_{325} . **b**, Self-accelerating beam generator B_{325}. **c**, Metahologram H_{325}.

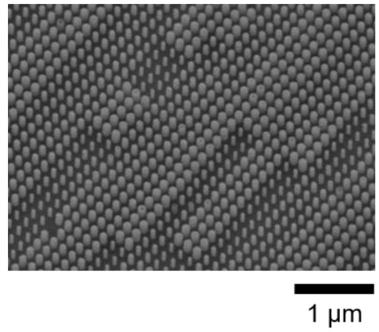

Fig. S9. Scanning electron micrograph (viewing angle: 20°) of selected areas of polarization-independent metahologram designed for operation at λ_0 = 266 nm, H_{266}.

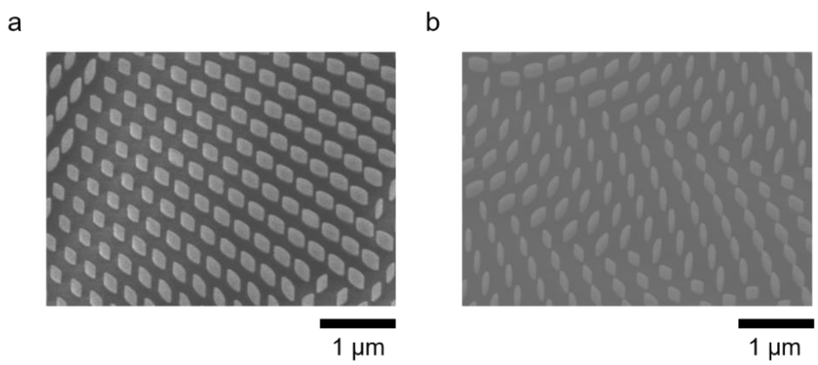

Fig. S10. Scanning electron micrograph (viewing angle: 20°) of selected areas of spin-multiplexed metasurfaces designed for operation at λ_0 = 364 nm. **a**, Metahologram $\mathrm{H}_{364}^{\mathrm{spin}}$. **b**, Self-accelerating beam generator $\mathrm{B}_{364}^{\mathrm{spin}}$.

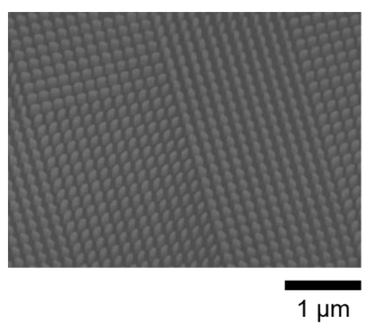

Fig. S11. Scanning electron micrograph (viewing angle: 20°) of selected areas of spin-multiplexed metahologram designed for operation at λ_0 = 266 nm, $\mathrm{H}_{266}^{\mathrm{spin}}$.

VIII. Design of the polarization-independent metasurfaces

The transmittance, T, and induced phase shift, φ, of an array of cylindrical pillars of diameter D, height H, and lattice spacing P, under plane-wave normal illumination at wavelengths λ_0 = 364 nm, 325 nm, and 266 nm, respectively, are computed using the finite-difference-time-domain (FDTD) simulations with periodic boundary conditions. Given a constant lattice spacing P over the entire metasurface, the function of the cylindrical pillars is to provide a relative propagation phase shift of up to $\varphi_{max} - \varphi_{min}$ = 2π, between the phase φ_{min} induced by the smallest-diameter pillar array (having a small filling factor compared to P, yielding a through-array propagation index $n_{min} \approx 1$, close to the refractive index of air) and the phase φ_{max} induced by the largest-diameter pillar array (having a larger filling factor compared to P, yielding a through-array propagation index $n_{max} \approx 2.1$, close to averaged index of refraction n of HfO_2 in the UV regime). This requirement sets a lower limit on possible values of H of $H_{min} = \lambda_0 / (n_{max} - n_{min}) \approx \lambda_0$.

Other constraints help to limit the extent of parameter space necessary to explore during the metasurface design process: (1) to avoid diffraction of transmitted light, the upper limit of P, P_{max}, is chosen such that $P_{max} \leq \lambda_0$; (2) to stay within the process tolerance of the Damascene lithography, the minimum value of D, D_{min}, is chosen such that D_{min} = 50 nm; (3) to maintain the mechanical stability of the resist template, the maximum possible value of D is chosen as ($P - 40$ nm). For each targeted free-space operation wavelength λ_0, different combinations of H, P are surveyed subject to the above requirements, along with the additional constraints that: (1) $\varphi(D) - \varphi(D_{min})$ span at least the full range of [0 2π], as D increases between D_{min} and a value $D_{max} \leq$ (P – 40 nm), where $\varphi(D_{max})$ = 2π, and (2) the transmittance T maintains a high and relatively constant value as D varies over the same range. Sets (H, P, D_{min}, and D_{max}) satisfying all those conditions are obtained for each of the targeted free-space operation wavelength, λ_0 = 364 nm, 325 nm, and 266 nm, of (550, 200, 50, 160), (500, 190, 50, 150), and (400, 150, 50, 110), respectively, where all values are expressed in nanometers (Fig. S12).

For each implemented polarization-independent metasurface device, the pillar height H and lattice spacing P are chosen based on the metasurface operating wavelength λ_0. The diameter of each nano-cylinder over the metasurface plane is chosen such that the induced phase-shift $\varphi(D, x_c, y_c) = mod(\varphi^{PI}(x_c, y_c), 2\pi)$, where φ^{PI} is the required phase-shift profile for each metasurface, D is the diameter of the nanopillar, and (x_c, y_c) is the center position of each cylinder. For all polarization-independent metasurface designs, 32 discretized phase levels are chosen for φ^{PI}.

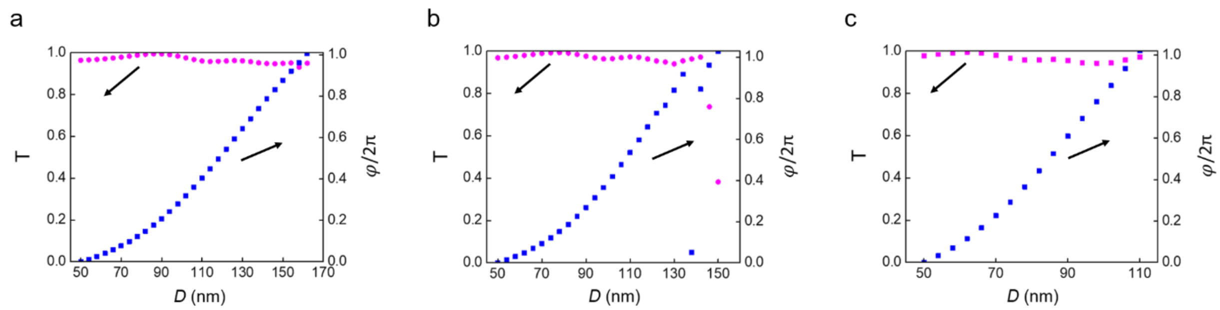

Fig. S12. Transmission intensity T and phase shift φ for an incident light of free-space wavelength λ_0 = 364 nm (a), 325 nm (b), and 266 nm (c), as a function of cylinder diameter *D*. For each free-space wavelength design (λ_0 = 364 nm, 325 nm, and 266 nm), a corresponding cylinder height (*H* = 550 nm, 500 nm, and 400 nm, respectively), sub-wavelength lattice spacing (*P* = 200 nm, 190 nm, and 150 nm, respectively), and maximum value of pillar diameter (D_{max} = 160 nm, 150 nm, and 110 nm, respectively) are chosen. For ease of display, the phase shift for pillar arrays with diameter *D* = 50 nm is set to zero for each design.

IX. Characterization procedure for metalenses L_{364} and L_{325}

A continuous wave (CW) laser beam (diameter: ≈ 5 mm) illuminates either metalens L_{364} (using wavelength λ_0 = 364 nm) or L_{325} (using wavelength λ_0 = 325 nm) at normal incidence, yielding a focused spot in the focal plane of the metalens. The intensity distribution of the image in this plane is captured using a custom-built imaging system including an NA = 0.75 objective and an EMCCD camera. The magnification of the system, characterized at each wavelength by translating the focal spot within the field of view of the objective using a calibrated stage, is measured to be 420 and 617 for λ_0 = 364 and 325 nm, respectively. The physical size of the focal spot projected by metalenses L_{364} and L_{325} is then derived based on the CCD pixel size and magnification calibrated for respective operating wavelengths.

X. Characterization procedure for self-accelerating beam generators B_{364} and B_{325}

A continuous wave (CW) laser beam (diameter: ≈ 5 mm) illuminates either self-accelerating beam generator B_{364} (using wavelength λ_0 = 364 nm) or B_{325} (using wavelength λ_0 = 325 nm) at the normal incidence. The intensity distributions of the generated self-accelerating beams in selected *z*-planes beyond the metasurface are recorded using custom-built imaging system including an NA = 0.75 objective and an EMCCD camera. Specific *z*-planes are addressed using a stage which translates the metasurface relative to the camera, along the direction of the laser beam. A 500-μm-diameter aperture is placed behind each metasurface substrate to completely separate the generated self-accelerating beam from directly transmitted light leaking around the edges of the metasurface (which occupies a square area of side length 270 μm). The physical size of the captured intensity profile is determined by comparison to the image of the area occupied by the metasurface.

XI. Designed phase shift profiles for metaholograms H_{364}, H_{325}, and H_{266}

The Gerchberg-Saxton algorithm[4] is employed to calculate the respective metasurface phase shift profiles, $\varphi^{H}_{364}(x, y, \lambda_0)$, $\varphi^{H}_{325}(x, y, \lambda_0)$, and $\varphi^{H}_{266}(x, y, \lambda_0)$, required to produce a holographic "NIST" image at three different operation wavelengths λ_0 = 364 nm, 325 nm, and 266 nm (shown in Fig. S13 and implemented, respectively, by metaholograms H_{364}, H_{325}, and H_{266}).

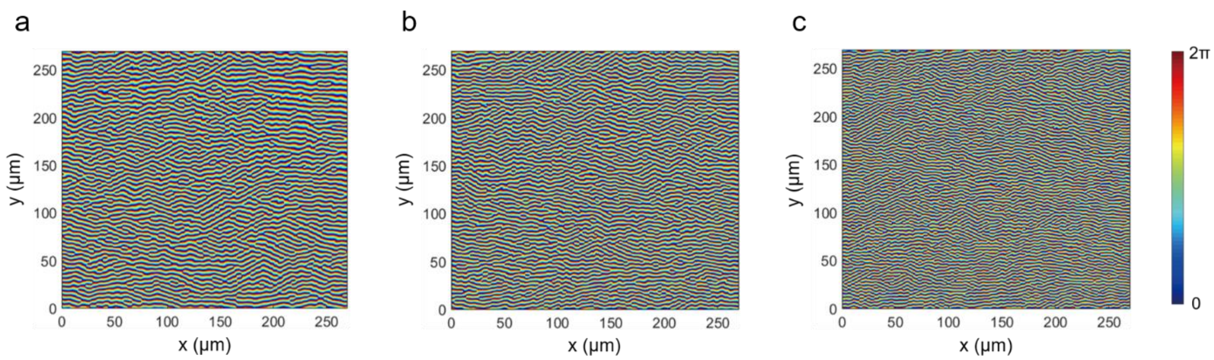

Fig. S13. Metasurface phase shift profiles, $\varphi^{H}_{364}(x, y, \lambda_0)$, $\varphi^{H}_{325}(x, y, \lambda_0)$, and $\varphi^{H}_{266}(x, y, \lambda_0)$, designed to produce a "NIST" holographic image for normal-incidence, plane-wave illumination at λ_0 = (a) 364 nm, (b) 325 nm, and (c) 266 nm (implemented by polarization independent metaholograms, H_{364}, H_{325}, and H_{266}, respectively).

XII. Characterization procedure for metaholograms $\mathbf{H_{364}}$ and $\mathbf{H_{325}}$

A continuous wave (CW) laser beam (diameter: ≈ 5 mm) illuminates either metahologram H_{364} (using wavelength λ_0 = 364 nm) or H_{364} (using wavelength λ_0 = 325 nm) at normal incidence. An EMCCD camera is placed in the hologram formation plane located 40 mm beyond the metahologram, to directly record the projected holographic image. A 500-μm-diameter aperture is placed behind the metasurface substrate to completely separate the generated holographic image (projected with a 3-mm lateral offset) from directly transmitted light leaking around the edges of the metasurface (which occupies a square area of side length 270 μm).

XIII. Characterization procedure for metahologram $\mathbf{H_{266}}$

A normally incident, 266-nm pulsed laser (pulse duration: ≈ 5 ns, repetition rate: 10 Hz, beam diameter: ≈ 6 mm) is used to directly illuminate the polarization-independent metahologram H_{266}. A piece of fluorescent white paper is placed in the hologram formation plane located 40 mm beyond each metahologram and imaged with a custom-built imaging system including a lens and a CCD camera. Holographic images are recorded for device H_{266} under linearly-polarized illumination. 500 images each are recorded and averaged, in each case, with and without laser illumination to subtract background and dark counts from the recorded image as well as to reduce random image noise. A 500-µm-diameter aperture is placed behind each metasurface substrate to completely separate the generated holographic image (projected with a 3-mm lateral offset) from directly transmitted light leaking around the edges of the metasurface (which occupies a square area of side length 270 um). The physical size of the captured holographic image is determined by comparison to the image of an object of known size placed in the plane of the fluorescent white paper.

To verify that the utilized fluorescent transduction scheme is linear, images are recorded under illumination with different laser powers. The ratio of the fluorescence power integrated over the holographic image to that integrated over the image of the directly transmitted beam is found to be invariant as a function of incident laser power, over the full range of power levels used for the experiment.

XIV. Design of spin-multiplexed metasurfaces

The spin-multiplexed metasurfaces implemented in this work impart independent phase shift profiles on an incident beam depending on its handedness, namely left-handed circularly polarized (LCP) and right-handed circularly polarized (RCP). Let the LCP and RCP state be represented by Jones Vectors $|L\rangle = \begin{bmatrix} 1 \\ -i \end{bmatrix}$ and $|R\rangle = \begin{bmatrix} 1 \\ i \end{bmatrix}$, respectively, and the wave transformation characteristics of the spin-multiplexed metasurface be described by a Jones Matrix $J(x, y)$.

$J(x, y)$ then satisfies the pair of equations

$$\begin{cases} e^{i\varphi_1(x,y)}|R\rangle = J(x,y)|L\rangle & (1) \\ e^{i\varphi_2(x,y)}|L\rangle = J(x,y)|R\rangle & (2) \end{cases}$$

where $\varphi_1(x, y)$ and $\varphi_2(x, y)$ denote the phase shift profiles of the emerging right-handed and left-handed light, for left-handed and right-handed illumination, respectively.

The Jones Matrix $J(x, y)$ can then be written as:

$$J(x,y) = \begin{bmatrix} e^{i\varphi_1(x,y)} & e^{i\varphi_2(x,y)} \\ -ie^{i\varphi_1(x,y)} & ie^{i\varphi_2(x,y)} \end{bmatrix} \begin{bmatrix} 1 & 1 \\ -i & i \end{bmatrix}^{-1} \qquad (3)$$

Such a Jones Matrix can be realized using uniaxial (geometrically birefringent) nanostructures providing different phase shifts along their two orthogonal principle axes (here denoted as I and II)[5]. In this study, we use HfO_2 nanopillars of in-plane elliptical cross-sections to provide such birefringent functionality. To implement the Jones Matrix of Equation (3), the phase shifts experienced by the constituent linear polarization components of the circularly-polarized incident light decomposed along principle axes I and II must satisfy $\delta_I(x, y) = [\varphi_1(x, y) + \varphi_2(x, y)]/2$, and $\delta_{II}(x,y) = -\pi + [\varphi_1(x,y) + \varphi_2(x,y)]/2$, respectively. In addition, the orientation angle $\theta(x,y)$ of the cylinder's principle axis *II* must satisfy:

$$\theta(x,y) = [\varphi_1(x,y) - \varphi_2(x,y)]/4 \qquad (4)$$

To design spin-multiplexed metasurfaces operating at λ_0 = 364 nm, the transmittance and phase shift for propagation of 364-nm-wavelength light, linearly-polarized either (1) parallel to one principle axis *I* (T_1 and Δ_1), or (2) parallel to the other principle axis *II* (T_2 and Δ_2) of an array of elliptical HfO_2 pillars (of orthogonal principle axis lengths D_1 and D_2, height *H*, and lattice spacing *P*) are computed using the finite-difference-time-domain (FDTD) simulations with periodic boundary conditions. For a given pillar height *H* and lattice spacing *P*, D_1 and D_2 are iteratively varied to identify orthogonal principle axis combinations simultaneously leading to $|\Delta_1 - \Delta_2| \approx \pi$ and $T_1 \approx T_2$, in other words, half-wave-plate-like operation. To confine the search to a computationally reasonable parameter space, the targeted values of Δ_1 are restricted to eight discrete, equally spaced values spanning the full 0 to 2π range (modulo 2π), required for arbitrary hologram implementation. The above constraints are found to be achievable with eight different nanopillar arrays, each of which are composed of elliptical nanopillars (denoted as C_1^{364} to C_8^{364}) having uniform height *H* = 500 nm, uniform spacing *P* = 330 nm, and discrete principle axis combinations, (D_1, D_2), expressed in nanometers, of (70, 190), (80, 240), (90, 260), (100, 270), (190, 70), (240, 80), (260, 90), and (270, 100), respectively (where half of the set is mathematically degenerate under an in-plane coordinate system rotation by 90°). The simulated orthogonal principle axis transmittance combinations, (T_1, T_2), are (93.4 %, 62.5 %), (93.1 %, 68.1 %), (95.6 %, 61.4 %), (89.1 %, 51.5 %), (62.5 %, 93.4 %), (68.1 %, 93.1 %), (61.4 %, 95.6 %), and (51.5 %, 89.1 %) for arrays composed exclusively of pillars C_1^{364} to C_8^{364}, respectively. The simulated orthogonal principle axis phase shift combinations, (Δ_1, Δ_2), are (0.82π, 2π), (1.35π, 0.41π), (1.58π, 0.67π), (1.87π, 0.87 π), (2π, 0.82π), (0.41π, 1.35π), (0.67π, 1.58π), and (0.87π, 1.87π) for the corresponding arrays.

To implement each spin-multiplexed metasurface operating at 364 nm (metahologram $\mathrm{H}_{364}^{\mathrm{spin}}$ and self-accelerating beam generator $\mathrm{B}_{364}^{\mathrm{spin}}$), the required phase shifts induced along the two orthogonal principle axes of an elliptical pillar of center position (x_c, y_c), $\phi_I[x_c, y_c]$ and $\phi_{II}[x_c, y_c]$, are calculated as $\phi_I[x_c, y_c] = mod((\varphi_1(x_c, y_c) + \varphi_2(x_c, y_c))/2\,, 2\pi)$ and $\phi_{II}[x_c, y_c] = mod(-\pi + (\varphi_1(x_c, y_c) + \varphi_2(x_c, y_c))/2\,, 2\pi)$, respectively. ϕ_I is then compared to each element $\emptyset_{ref,i}$ of a discretized reference phase set $\emptyset_{ref} = \{\pi, 1.25\pi, 1.5\pi, 1.75\pi, 2\pi, 0.25\pi, 0.5\pi, 0.75\pi\}$, in order to identify the closest element to C_i^{364} (in other words, the index *i* such that $|\emptyset_{ref,i} - \phi_I| \leq 0.125\pi$ is satisfied). The resulting index *i* then identifies the specific nanopillar $C_i^{364} \in \{C_1^{364}, \cdots, C_8^{364}\}$ providing the optimal choice for metahologram constituent nanopillar at position (x_c, y_c). For each of such choice, the orientation angle $\theta[x_c, y_c]$ of the cylinder's principle axis *II* is set to $\theta[x_c, y_c] = mod((\varphi_1(x_c, y_c) - \varphi_2(x_c, y_c))/4\,, 2\pi)$.

Following the same design procedure, the spin-multiplexed metasurfaces operating at λ_0 = 266 nm can be implemented using a pillar library which consists of eight distinct elliptical nanopillars (denoted as C_1^{266} to C_8^{266}) having uniform height *H* = 480 nm, uniform spacing *P* = 160 nm, and eight discrete principle axis combinations, (D_1, D_2), expressed in nanometers, of (118, 58), (126, 62), (126, 70), (118, 50), (58, 118), (62, 126), (70, 126), and (118, 50) respectively (where half of the set is mathematically degenerate under an in-plane coordinate system rotation by 90°). The simulated orthogonal principle axis transmittance combinations, (T_1, T_2), are (93.4 %, 99.5 %), (94.4 %, 98.5 %), (94.8 %, 94.9 %), (97.8 %, 96.6 %), (99.5 %, 93.4 %), (98.5 %, 94.4 %), (94.9 %, 94.8 %), and (96.6 %, 97.8 %) for arrays composed exclusively of pillars C_1^{266} to C_8^{266}, respectively. The simulated orthogonal principle axis phase shift combinations, (Δ_1, Δ_2), are (1.02π, 2π), (1.21π, 0.26 π), (1.54π, 0.48π), (1.74π, 0.8 π), (2π, 1.02 π), (0.26π, 1.21π), (0.48π, 1.54π), and (0.8π, 1.74π) for the corresponding arrays. The two independent phase shift profiles associated with the spin-multiplexed metahologram, $\mathrm{H}_{266}^{\mathrm{spin}}$, are implemented by choosing, at each position of the metasurface, the optimal nanopillar $C_i^{266} \in \{C_1^{266}, \cdots, C_8^{266}\}$, according to the algorithm outlined in earlier part of this section.

XV. Characterization procedure for spin-multiplexed self-accelerating beam generator $\mathbf{B}_{\mathbf{364}}^{\mathbf{spin}}$

To characterize the spin-multiplexed self-accelerating beam generator $\mathrm{B}_{364}^{\mathrm{spin}}$, a normally incident, 364-nm continuous wave (CW) laser beam (beam diameter: ≈ 5 mm) is used to illuminate the device, and a linear polarizer and a quarter-wave plate (of center wavelength 355 nm) are used in addition to control the handedness of the illuminating light. The intensity distributions of the generated self-accelerating beams in selected *z*-planes beyond the metasurface are recorded using custom-built imaging system including an NA = 0.75 objective and an EMCCD camera, under LCP and RCP illumination, respectively. Specific *z*-planes (ranging from 2.5 mm to 4.5 mm, with an increment of 0.5 mm, for LCP illumination, and ranging from 4.5 mm to 10.5 mm, with an increment of 1.5 mm, for RCP illumination) are addressed using a stage which translates the metasurface relative to the camera, along the direction of the laser beam. A 500-μm-diameter aperture is placed behind the metasurface substrate to completely separate the generated self-accelerating beam from directly transmitted light leaking around the edges of the metasurface (which occupies a square area of side length 330 μm). The physical size of the captured intensity profile is determined by comparison to the image of the area occupied by the metasurface.

The experimental SAB generated by the device, under LCP and RCP illumination, respectively, exhibits a diffraction-free character with *xy*-plane intensity distributions similar to the targeted intensity distributions (Figs. S14 and S15), numerically computed using the angular spectrum representation method[4], assuming an ideal metasurface realization having both the designed phase shift profile φ^B and an unity transmittance T.

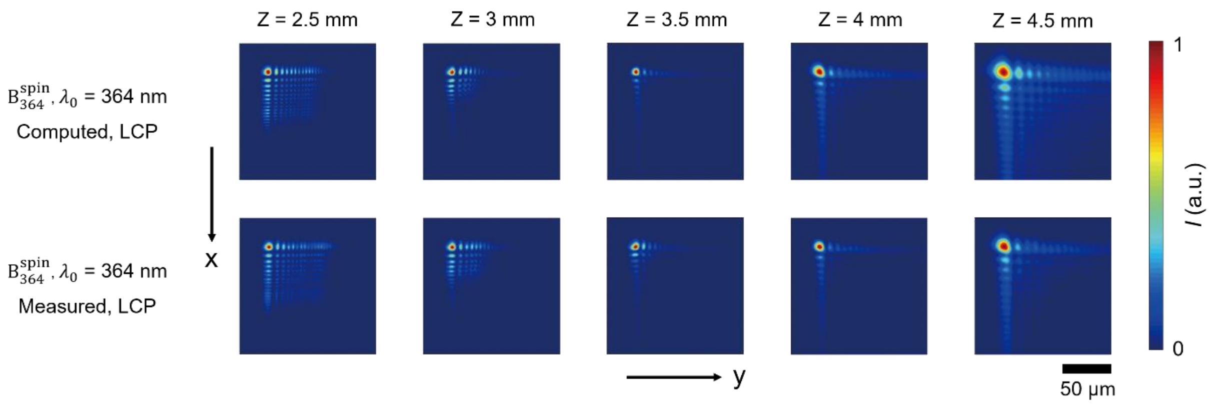

Fig. S14. Computed and measured *xy*-plane intensity distributions (normalized) at different *z* planes for device B_{364}^{spin} at its designated wavelength of operation under LCP illumination. Each distribution is displayed over an equal square area of side length 140 µm, but shifted along the -*xy* direction as a function of increasing *z*, such that the center of the main lobe maintains an invariant position within each image.

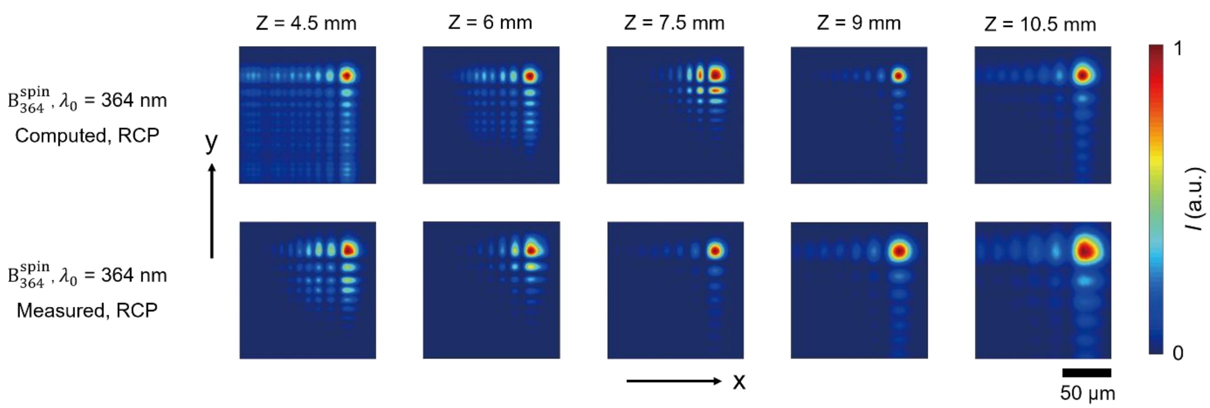

Fig. S15. Computed and measured *xy*-plane intensity distributions (normalized) at different *z* planes for device B_{364}^{spin} at its designated wavelength of operation under RCP illumination. Each distribution is displayed over an equal square area of side length 140 µm, but shifted along the *xy* direction as a function of increasing *z*, such that the center of the main lobe maintains an invariant position within each image.

XVI. Discussion of reduced device efficiency under LCP illumination for $\mathbf{B}_{\mathbf{364}}^{\mathbf{spin}}$

The spin-multiplexed SAB generator, $\mathrm{B}_{364}^{\mathrm{spin}}$, occupies a square area of side length l = 330 µm. Two distinct phase shift profiles, $\varphi^{LCP}(x, y, \lambda_0) = mod\left(-\frac{8\pi}{3\lambda_0}\sqrt{16}\left(x^{\frac{3}{2}} + y^{\frac{3}{2}}\right), 2\pi\right)$ and $\varphi^{RCP}(x, y, \lambda_0) = mod\left(-\frac{8\pi}{3\lambda_0}\sqrt{2.25}\left((l-x)^{\frac{3}{2}} + (l-y)^{\frac{3}{2}}\right), 2\pi\right)$, are targeted for device operation, in order to yield SABs exiting the metasurface from opposite corners and following different trajectories, $y = x = -d_1 = -16z^2$, and $(y - l) = (x - l) = d_2 = 2.25z^2$, under LCP and RCP illumination, respectively.

The targeted phase shift profiles for LCP and RCP illuminations, $\varphi^{LCP}(x, y)$ and $\varphi^{RCP}(x, y)$, are plotted in Fig. S16. For the purpose of clarity, the phase shift profiles are only displayed over a 50 µm by 50 µm square area with one corner at (0, 0) and (330 µm, 330 µm) for φ^{LCP} and φ^{RCP}, respectively. It can be easily seen that φ^{LCP} exhibits a higher spatial gradient than φ^{RCP} and varies rapidly over the space.

The implemented metasurface consists of nanopillars of elliptical in-plane cross-sections, that are arrayed in a square lattice with lattice spacing of 330 nm. The size and orientation of each nanopillar is chosen based on the targeted values of φ^{LCP} and φ^{RCP} in the center position of the lattice, as well as the associated design library. Consequently, the spatially-continuously-varying $\varphi^{LCP}(x, y)$ and $\varphi^{RCP}(x, y)$ are now realized (approximated) by discrete phase values over the metasurface plane. Due to its higher spatial gradient (faster spatial variation), φ^{LCP} is less ideally implemented compared to φ^{RCP}, and this leads to the reduced metasurface efficiency under LCP illumination.

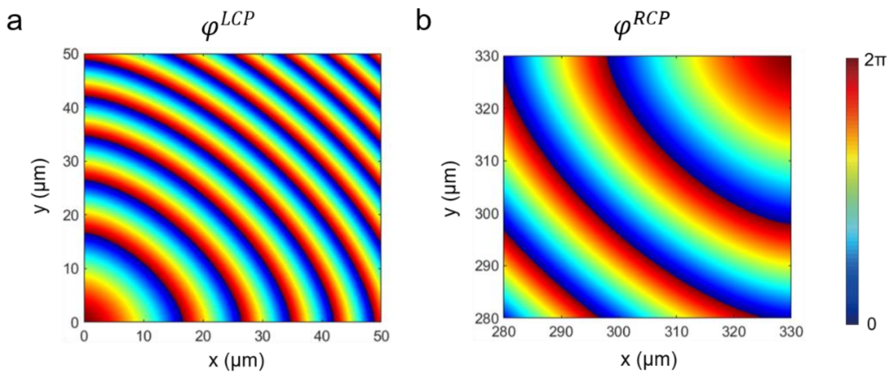

Fig. S16. Targeted phase shift profiles, $\varphi^{LCP}(x, y)$ and $\varphi^{RCP}(x, y)$, for the spin-multiplexed SAB generator. For the purpose of clarity, the phase shift profiles are only displayed over a 50 μm by 50 μm square area with one corner at (0, 0) and (330 μm, 330 μm) for φ^{LCP} and φ^{RCP}, respectively.

XVII. Implementation of spin-multiplexed metahologram $\mathbf{H}_{\mathbf{364}}^{\mathbf{spin}}$

A spin-multiplexed metahologram, $\mathrm{H}_{364}^{\mathrm{spin}}$, occupying a square area of side length 330 µm, is implemented for operation at λ_0 = 364 nm. Different phase profiles (Fig. S17), $\varphi_{364,\mathrm{LCP}}^{\mathrm{H,spin}}(x, y, \lambda_0)$ and $\varphi_{364,\mathrm{RCP}}^{\mathrm{H,spin}}(x, y, \lambda_0)$, all based on the Gerchberg-Saxton algorithm, are calculated for projecting a holographic "NIST" image (for LCP illuminating light) and "NJU" image (for RCP illuminating light), all located in the z = 40 mm plane, with an offset of $y = -3$ mm (Fig. S18).

A normally incident, 364-nm continuous wave (CW) laser beam (beam diameter: ≈ 5 mm) is used to illuminate the metahologram, and a linear polarizer and a quarter-wave plate (with a center wavelength of 355 nm) are used in addition to control the handedness of the illuminating light. An EMCCD camera is placed in the hologram formation plane located 40 mm beyond the metahologram to directly record the projected holographic images under LCP and RCP illumination, respectively. A 500-µm-diameter aperture is placed behind the metahologram substrate to completely separate the generated holographic image (projected with a 3-mm lateral offset) from directly transmitted light leaking around the edges of the metasurface (which occupies a square area of side length 330 µm).

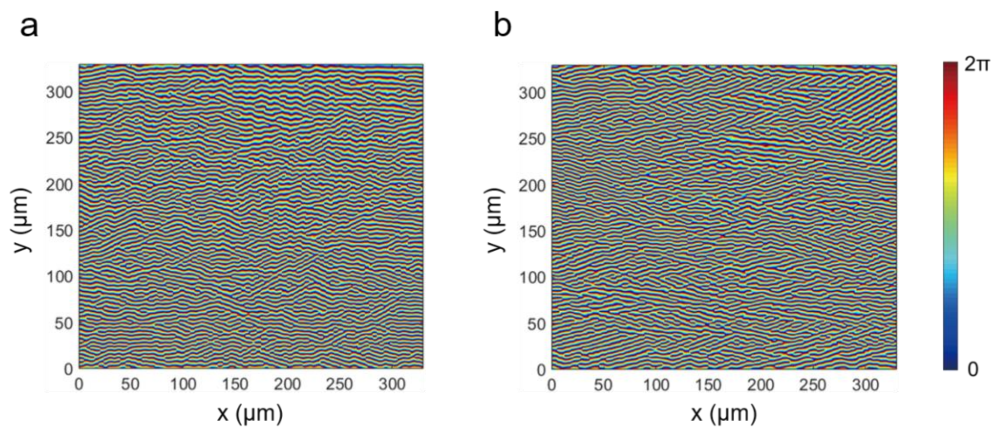

Fig. S17. Metasurface phase shift profiles, $\varphi^{\mathrm{H,spin}}_{364,\mathrm{LCP}}(\mathrm{x}, \mathrm{y}, \lambda_0)$ and $\varphi^{\mathrm{H,spin}}_{364,\mathrm{RCP}}(\mathrm{x}, \mathrm{y}, \lambda_0)$, designed to project a "NIST" (a) and "NJU" (b) holographic image in the *z* = 40 mm plane, under normal-incidence, plane-wave illumination at λ_0 = 364 nm (implemented by spin-multiplexed metahologram $\mathrm{H}^{\mathrm{spin}}_{364}$).

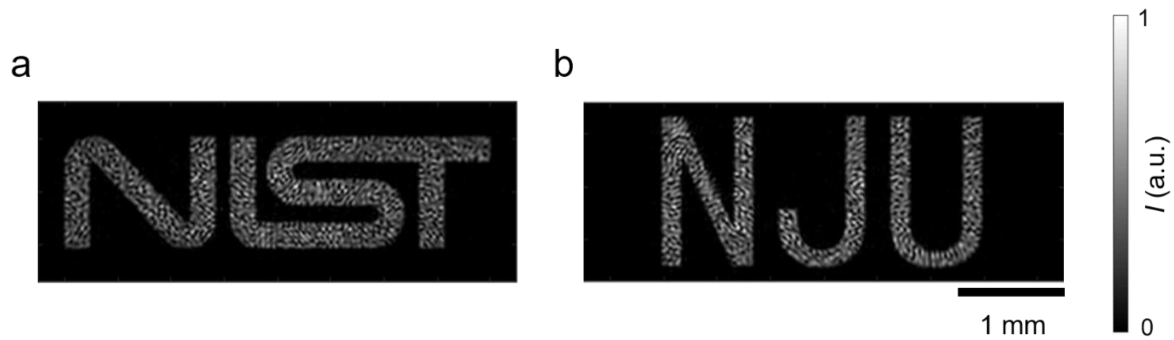

Fig. S18. Targeted holographic images in the *z* = 40 mm plane, numerically computed assuming an ideal metahologram realization having an unity transmittance, and either (a) phase shift profile $\varphi^{\mathrm{H,spin}}_{364,\mathrm{LCP}}(x, y, \lambda_0)$ shown in Fig. S17a or (b) phase shift profile $\varphi^{\mathrm{H,spin}}_{364,\mathrm{RCP}}(x, y, \lambda_0)$ shown in Fig. S17b, under normal-incidence, plane-wave illumination at λ_0 = 364 nm.

XVIII. Implementation of spin-multiplexed metahologram $\mathbf{H}_{\mathbf{266}}^{\mathbf{spin}}$

Two different phase shift profiles over 320-µm-square areas (Fig. S19), $\varphi_{266,\mathrm{LCP}}^{\mathrm{H,spin}}(x, y, \lambda_0)$ and $\varphi_{266,\mathrm{RCP}}^{\mathrm{H,spin}}(x, y, \lambda_0)$, are calculated using the Gerchberg-Saxton algorithm to achieve projection of distinct holographic images under normal-incidence, plane-wave illumination at λ_0 = 266 nm, namely, "deep" and "UV" images, respectively, in the *z* = 40 mm plane, with an offset $y = -3$ mm (Fig. S20).

A normally incident, 266-nm pulsed laser (pulse duration: ≈ 5 ns, repetition rate: 10 Hz, beam diameter: ≈ 6 mm) is used to illuminate the spin-multiplexed metahologram $\mathrm{H}_{266}^{\mathrm{spin}}$. In addition, a linear polarizer and a quarter-wave plate (with a center wavelength of 266 nm) are used to control the handedness of the illuminating light. A piece of fluorescent white paper is placed in the hologram formation plane located 40 mm beyond the metahologram and imaged with a custom-built imaging system including a lens and a CCD camera. Holographic images are recorded for device $\mathrm{H}_{266}^{\mathrm{spin}}$ under LCP and RCP illumination, respectively. 500 images are recorded and averaged, in each case, with and without laser illumination to subtract background and dark counts from the recorded image as well as to reduce random image noise. A 500-µm-diameter aperture is placed behind each metasurface substrate to completely separate the generated holographic image (projected with a 3-mm lateral offset) from directly transmitted light leaking around the edges of the metasurface (which occupies a square area of side length 320 µm). The physical size of the captured holographic image is determined by comparison to the image of an object of known size placed in the plane of the fluorescent white paper.

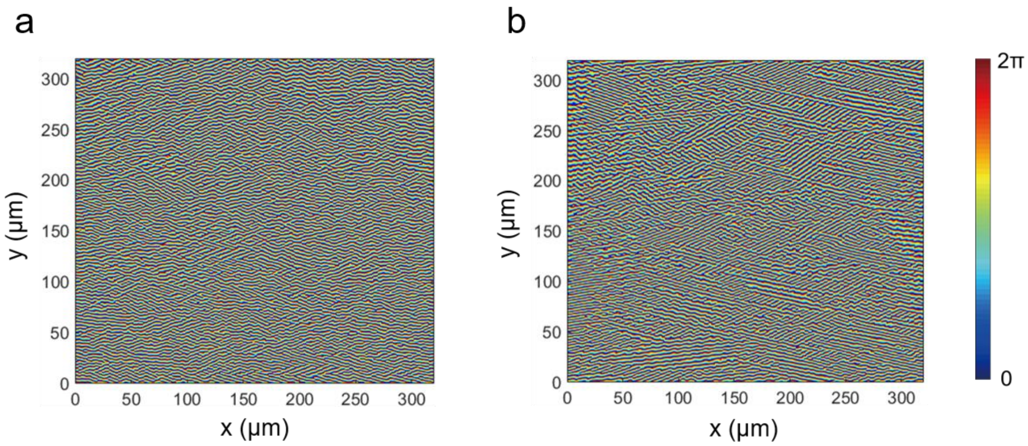

Fig. S19. Metasurface phase shift profiles, $\varphi^{\mathrm{H,spin}}_{266,\mathrm{LCP}}(x, y, \lambda_0)$ and $\varphi^{\mathrm{H,spin}}_{266,\mathrm{RCP}}(x, y, \lambda_0)$, designed to project a "deep" (a) and "UV" (b) holographic image in the *z* = 40 mm plane, under normal-incidence, plane-wave illumination at λ_0 = 266 nm (implemented by spin-multiplexed metahologram $\mathrm{H}^{\mathrm{spin}}_{266}$).

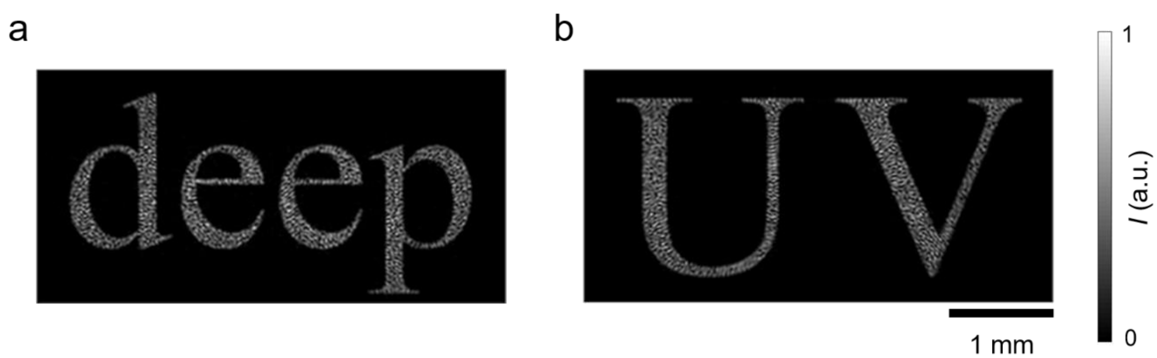

Fig. S20. Targeted holographic images in the *z* = 40 mm plane, numerically computed assuming an ideal metahologram realization having an unity transmittance, and either (a) phase shift profile $\varphi^{\mathrm{H,spin}}_{266,\mathrm{LCP}}(x, y, \lambda_0)$ shown in Fig. S19a or (b) phase shift profile $\varphi^{\mathrm{H,spin}}_{266,\mathrm{RCP}}(x, y, \lambda_0)$ shown in Fig. S19b, under normal-incidence, plane-wave illumination at λ_0 = 266 nm.

References:

1. Hilfiker, J. N., Singh, N., Tiwald, T., Convey, D., Smith, S. M., Baker, J. H., Tompkins, H. G. Survey of methods to characterize thin absorbing films with Spectroscopic Ellipsometry. *Thin Solid Films* **516**, 7979 (2008).

2. Zhang, C., Hong, N., Ji, C., Zhu, W., Chen, X., Agrawal, A., Zhang, Z., Tiwald, T. E., Schoeche, S., Hilfiker, J. N., Guo, L. J., Lezec, H. J. Robust extraction of hyperbolic metamaterial permittivity using total internal reflection ellipsometry. *ACS Photonics* **5**, 2234 (2018).

3. Novotny, L., Hecht, B. Principles of Nano-Optics Ch. 3 (Cambridge Univ. Press, Cambridge, 2006).

4. Gerchberg, R. W., Saxton, W. O. A practical algorithm for the determination of the phase from image and diffraction plane pictures. *Optik* **35**, 237 (1972).

5. Balthasar Mueller, J. P., Rubin, N. A., Devlin, R. C., Groever, B., Capasso, F. Metasurface polarization optics: independent phase control of arbitrary orthogonal states of polarization. *Phys. Rev. Lett.* **118**, 113901 (2017).